

1 **Role of spike in the pathogenic and antigenic behavior of SARS-CoV-2 BA.1**

2 **Omicron**

3 Da-Yuan Chen^{1,2}, Devin Kenney^{2,3}, Chue Vin Chin^{1,2}, Alexander H. Tavares^{1,2}, Nazimuddin
4 Khan^{1,2}, Hasahn L. Conway^{1,2}, GuanQun Liu⁴, Manish C. Choudhary^{5,6}, Hans P. Gertje², Aoife
5 K. O’Connell², Darrell N. Kotton^{7,8}, Alexandra Herrmann⁹, Armin Ensser⁹, John H. Connor^{2,3},
6 Markus Bosmann^{10,11,12}, Jonathan Z. Li^{5,6}, Michaela U. Gack⁴, Susan C. Baker¹³, Robert N.
7 Kirchdoerfer¹⁴, Yachana Kataria¹¹, Nicholas A. Crossland^{2,11}, Florian Douam^{2,3}, Mohsan
8 Saeed^{1,2#}

9
10 1. Department of Biochemistry, Boston University School of Medicine, Boston, MA, USA

11 2. National Emerging Infectious Diseases Laboratories, Boston University, Boston, MA,
12 USA

13 3. Department of Microbiology, Boston University School of Medicine, Boston, MA, USA

14 4. Cleveland Clinic Florida Research and Innovation Center, Port St. Lucie, FL, USA

15 5. Brigham and Women’s Hospital, Boston, MA, USA

16 6. Harvard Medical School, Cambridge, MA, USA

17 7. Center for Regenerative Medicine of Boston University and Boston Medical Center,
18 Boston, MA, USA

19 8. The Pulmonary Center and Department of Medicine, Boston University School of
20 Medicine, Boston, MA, USA

- 21 9. Institute of Clinical and Molecular Virology, University Hospital Erlangen, Friedrich-
22 Alexander Universität Erlangen-Nürnberg, Erlangen, Germany
- 23 10. Pulmonary Center, Boston University School of Medicine, MA, USA
- 24 11. Department of Pathology and Laboratory Medicine, Boston University School of
25 Medicine, MA, USA
- 26 12. Center for Thrombosis and Hemostasis, University Medical Center of the Johannes
27 Gutenberg-University, Mainz, Germany
- 28 13. Department of Microbiology and Immunology, and Infectious Disease and Immunology
29 Research Institute, Stritch School of Medicine, Loyola University, Chicago, Maywood, IL,
30 USA
- 31 14. Department of Biochemistry, College of Agricultural and Life Sciences, University of
32 Wisconsin, Madison, WI, USA

33 #Correspondence: msaeed1@bu.edu

34

35

36

37

38

39

40

41 **The recently identified, globally predominant SARS-CoV-2 Omicron variant (BA.1) is**
42 **highly transmissible, even in fully vaccinated individuals, and causes attenuated disease**
43 **compared with other major viral variants recognized to date¹⁻⁷. The Omicron spike (S)**
44 **protein, with an unusually large number of mutations, is considered the major driver of**
45 **these phenotypes^{3,8}. We generated chimeric recombinant SARS-CoV-2 encoding the S**
46 **gene of Omicron in the backbone of an ancestral SARS-CoV-2 isolate and compared this**
47 **virus with the naturally circulating Omicron variant. The Omicron S-bearing virus robustly**
48 **escapes vaccine-induced humoral immunity, mainly due to mutations in the receptor-**
49 **binding motif (RBM), yet unlike naturally occurring Omicron, efficiently replicates in cell**
50 **lines and primary-like distal lung cells. In K18-hACE2 mice, while Omicron causes mild,**
51 **non-fatal infection, the Omicron S-carrying virus inflicts severe disease with a mortality**
52 **rate of 80%. This indicates that while the vaccine escape of Omicron is defined by**
53 **mutations in S, major determinants of viral pathogenicity reside outside of S.**

54 As of March 2022, the successive waves of the coronavirus disease 2019 (COVID-19)
55 pandemic have been driven by five major SARS-CoV-2 variants, called variants of concern (VOC);
56 Alpha (B.1.1.7), Beta (B.1.351), Gamma (P.1), Delta (B.1.617.2 and AY lineages), and Omicron
57 (BA lineages)⁹. Omicron is the most recently recognized VOC that was first documented in South
58 Africa, Botswana, and in a traveler from South Africa in Hong Kong in November 2021 (GISAID
59 ID: EPI_ISL_7605742)^{10,11}. It quickly swept through the world, displacing the previously dominant
60 Delta variant within weeks and accounting for the majority of new SARS-CoV-2 infections by
61 January 2022¹²⁻¹⁶. Omicron has at least three lineages, BA.1, BA.2, and BA.3, with the former
62 being the most predominant lineage worldwide^{13,17-19}. BA.1 (hereinafter referred to as Omicron)

63 exhibits a remarkable escape from infection- and vaccine-induced humoral immunity^{4,5,20,21}.
64 Further, it is less pathogenic than other VOCs in humans and *in vivo* models of infection^{1-3,22-26}.
65 Omicron differs from the prototype SARS-CoV-2 isolate, Wuhan-Hu-1, by 59 amino acids; 37 of
66 these changes are in the S protein, raising the possibility that S is at the heart of Omicron's
67 pathogenic and antigenic behavior.

68 **Spike mutations only partially affect the replication of Omicron in cell culture**

69 The Omicron S protein carries 30 amino acid substitutions, 6 deletions, and one three-
70 amino acid-long insertion compared to Wuhan-Hu-1 (**Fig. 1a,b**). Twenty-five of these changes are
71 unique to Omicron relative to other VOCs, although some of them have been reported in waste
72 water and minor SARS-CoV-2 variants²⁷⁻²⁹. To test the role of the S protein in Omicron phenotype,
73 we generated a chimeric recombinant virus containing the S gene of Omicron (USA-Ih01/2021) in
74 the backbone of an ancestral SARS-CoV-2 isolate (GISAID EPI_ISL_2732373)³⁰ (**Fig. 1c**). To
75 produce this chimeric Omi-S virus, we employed a modified form of cyclic polymerase extension
76 reaction (CPER) (**Extended Data Fig. 1**) that yielded highly concentrated virus stocks, containing
77 $0.5-5 \times 10^6$ plaque-forming units (PFU) per ml, from transfected cells within two days of
78 transfection (**Fig. 1d,e**), obviating the need for additional viral amplification^{31,32}.

79 We first compared the infection efficiency of Omi-S with an ancestral virus and Omicron in
80 cell culture (**Fig. 2a**). For this, we infected ACE2/TMPRSS2/Caco-2³³ and Vero E6 cells with Omi-
81 S, a recombinant D614G-bearing ancestral virus (GISAID EPI_ISL_2732373)³⁰, and a clinical
82 Omicron isolate (USA-Ih01/2021) at a multiplicity of infection (MOI) of 0.01 and monitored viral
83 propagation by flow cytometry and the plaque assay. The ancestral virus [hereinafter referred to
84 as wild-type (WT)] and Omi-S spread fast in ACE2/TMPRSS2/Caco-2 cells, yielding 89% and

85 80% infected cells, respectively, at 24 hours post-infection (hpi) (**Fig. 2b**). In contrast, Omicron
86 replicated slower, leading to 48% infected cells at 24 hpi. A similar pattern was seen in Vero E6
87 cells, where 60% and 41% of cells were positive for WT and Omi-S, respectively, at 48 hpi, in
88 contrast to 10% positive cells for Omicron (**Fig. 2c**). The plaque assay showed that although both
89 Omi-S and Omicron produced lower levels of infectious virus particles compared with WT, the
90 viral titer of Omi-S was significantly higher than that of Omicron. In ACE2/TMPRSS2/Caco-2 cells,
91 Omi-S produced 5.1-fold ($p = 0.0006$) and 5.5-fold ($p = 0.0312$) more infectious particles than
92 Omicron at 12 hpi and 24 hpi, respectively (**Fig. 2d**). Similarly, in Vero E6 cells, the infectious
93 virus titers of Omi-S were 17-fold ($p = 0.0080$) and 11-fold ($p = 0.0078$) higher than that of Omicron
94 at 24 hpi and 48 hpi, respectively (**Fig. 2e**). The difference between viruses became less obvious
95 at later time points due to higher cytotoxicity caused by Omi-S compared with Omicron (**Fig. 2f**).
96 The higher infection efficiency of Omi-S relative to Omicron was also reflected in the plaque size;
97 while WT produced the largest plaques (~ 4.1 mm), the size of Omi-S plaques (~2.2 mm) was 2-
98 fold ($p < 0.0001$) larger than that of Omicron plaques (~1.1 mm) (**Fig. 2g**). These results indicate
99 that while mutations in the S protein influence the infection efficiency of Omicron, they do not fully
100 explain the infection behavior of Omicron in cell culture.

101 We next expanded our studies to lung epithelial cells, which are a major viral replication
102 site in patients with severe COVID-19. Accordingly, we employed human induced pluripotent stem
103 cell-derived lung alveolar type 2 epithelial (iAT2) cells. AT2 cells represent an essential cell
104 population in the distal lung and constitute one of the primary targets of SARS-CoV-2 infection³⁴⁻
105 ³⁶. We infected iAT2 cells, grown as an air-liquid interface (ALI) culture, at an MOI of 2.5 and
106 monitored the secretion of viral progeny on the apical interface of cells at 48 hpi and 96 hpi. In

107 congruence with the results obtained from cell lines, WT SARS-CoV-2 produced the highest levels
108 of infectious virus particles (**Fig. 2h**). Among the Omi-S and Omicron, the former yielded ~5-fold
109 ($p = 0.0008$) higher infectious viral titer at 48 hpi. The viral titers for WT and Omi-S decreased at
110 96 hpi compared with 48 hpi due to the cytopathic effect (CPE) of infection. However, no CPE
111 was seen for Omicron, leading to sustained production of infectious virions. Overall, these results
112 corroborate the conclusion that mutations in S do not fully account for the attenuated replication
113 capacity of Omicron in cultured human cells.

114 **Spike has an appreciable but minimal role in Omicron pathogenicity in K18-hACE2 mice**

115 To examine if Omi-S exhibits higher *in vivo* fitness compared with Omicron, we investigated
116 the infection outcome of Omi-S relative to WT SARS-CoV-2 and Omicron in K18-hACE2 mice. In
117 agreement with the published literature^{3,37-39}, intranasal inoculation of mice (aged 12-20 weeks)
118 with Omicron (10^4 PFU per animal) caused no significant weight loss, whereas inoculation with
119 WT virus triggered a rapid decrease in body weight with all animals losing over 20% of their initial
120 body weight by 8 days post-infection (dpi) (**Fig. 3a**). Importantly, 80% of animals infected with
121 Omi-S also lost over 20% of their body weight by 9 dpi (**Fig. 3a and Extended Data Fig. 2a**). The
122 evaluation of clinical scores (a cumulative measure of weight loss, abnormal respiration, aberrant
123 appearance, reduced responsiveness, and altered behavior) also revealed a similar pattern; while
124 Omicron-infected mice displayed little to no signs of clinical illness, the health of those infected
125 with WT and Omi-S rapidly deteriorated, with the former inflicting a more severe disease ($p =$
126 0.0102) (**Fig. 3b and Extended Data Fig. 2b**). Since SARS-CoV-2 causes fatal infection in K18-
127 hACE2 mice^{3,40,41}, we leveraged this situation to compare the animal survival after viral infection.
128 In agreement with the results of body-weight loss and clinical score, WT and Omi-S caused

129 mortality rates of 100% (6/6) and 80% (8/10), respectively. In contrast, all animals infected with
130 Omicron survived (**Fig. 3c**). These findings indicate that the S protein is not the primary
131 determinant of Omicron's pathogenicity in K18-hACE2 mice.

132 Next, we compared the virus propagation of Omi-S with Omicron and WT SARS-CoV-2 in
133 the lungs of K18-hACE2 mice. The mice (12-20 weeks old) were intranasally challenged with 10^4
134 PFU (7 mice per virus), and their lungs were collected at 2 and 4 dpi for virological and histological
135 analysis. Consistent with *in vitro* findings, the infectious virus titer in the lungs of WT-infected mice
136 was higher than that detected in mice infected with other two viruses (**Fig. 3d**). Notably however,
137 Omi-S-infected mice produced 30-fold ($p = 0.0286$) more infectious virus particles compared with
138 Omicron-infected mice at 2 dpi. The titer decreased at 4 dpi for WT- and Omi-S-infected mice, yet
139 it showed an increasing trend for Omicron-infected animals, pointing to the possibility of mild but
140 persistent infection by Omicron in K18-hACE2 mice.

141 To evaluate the viral pathogenicity in the lungs, we performed histopathological analysis of
142 the lung tissue of infected K18-hACE2 mice. As previously reported^{3,42}, an extensive near-diffused
143 immunoreactivity of the SARS-CoV-2 S protein was detected in lung alveoli of mice infected with
144 WT virus (**Fig. 3e**). In contrast, Omi-S and Omicron infection produced localized foci of alveolar
145 staining with fewer foci for Omicron compared with Omi-S. The most striking phenotype was seen
146 in bronchiolar epithelium. While Omi-S virus caused a severe bronchiolar infection with around
147 15-20% of bronchioles being positive for the S protein in all mice examined at 2 dpi, less than 1%
148 bronchioles were S-positive in Omicron-infected mice (**Fig. 3f**). Further, bronchiolar infection was
149 associated with epithelial necrosis in Omi-S-infected mice, as determined through serial
150 hematoxylin and eosin (H&E) section analysis, whereas no histological evidence of airway injury

151 was observed in Omicron-infected mice (**Extended Data Fig. 3**). This suggests that the replication
152 of Omicron in mice lungs, particularly in bronchioles, is substantially attenuated compared with
153 Omi-S, supporting our conclusion that mutations in the S protein are only partially responsible for
154 the attenuated pathogenicity of Omicron.

155 **Mutations in the spike RBM are major drivers of Omicron's escape from neutralization**

156 Next, we examined if Omi-S captures the immune escape phenotype of Omicron. A large
157 body of literature has demonstrated extensive escape of Omicron from vaccine-induced humoral
158 immunity^{4,10,43}. We compared the *in vitro* neutralization activity of sera obtained from vaccinated
159 individuals against the SARS-CoV-2 Washington isolate (USA-WA1/2020), Omi-S, and Omicron.
160 Sera collected within two months of the second dose of mRNA-1273 (Moderna mRNA vaccine; n
161 = 12) or BNT162b2 (Pfizer-BioNTech mRNA vaccine; n = 12) vaccine were included (**Extended**
162 **Data Table 1**). We performed a multicycle neutralization assay using a setting in which the virus
163 and neutralizing sera were present at all times, mimicking the situation in a seropositive individual.
164 All sera poorly neutralized Omicron, with 11.1-fold (range: 4.4- to 81.2-fold; $p < 0.0001$) lower half-
165 maximal neutralizing dilution (ND₅₀) for Omicron compared with WA1 (**Fig. 4a,b**). In fact, around
166 80% of samples failed to completely neutralize Omicron at the highest tested concentration
167 (**Extended Data Fig. 4**). Notably, Omi-S exhibited identical ND₅₀ values to Omicron (11.5-fold
168 lower than that of WA1; $p < 0.0001$) (**Fig. 4a,b**), suggesting that the Omicron S protein, when
169 incorporated into a WT virus, behaves the same way as in Omicron.

170 The SARS-CoV-2 S protein comprises two domains: the S1 domain, which interacts with
171 the ACE2 receptor, and the S2 domain, which is responsible for membrane fusion⁴⁴. Within the
172 S1 domain lie an N-terminal domain (NTD) and a receptor-binding domain (RBD), which harbors

173 the receptor-binding motif (RBM) that makes direct contact with the ACE2 receptor⁴⁵. The NTD of
174 Omicron S carries 11 amino acid changes, including 6 deletions and one three-amino acid-long
175 insertion, whereas the RBD harbors 15 mutations, 10 of which are concentrated in the RBM (**Fig.**
176 **1a,b**). Both NTD and RBD host neutralizing epitopes⁴⁶⁻⁵⁰, but the RBD is immunodominant and
177 represents the primary target of the neutralizing activity present in SARS-CoV-2 immune sera^{50,51}.
178 To determine if the neutralization resistance phenotype of Omicron is caused by mutations in a
179 particular S domain, we generated two groups of chimeric viruses. The first group comprised the
180 WA1 virus carrying the NTD, RBD, or RBM of Omicron (**Fig. 4c**), and the second group consisted
181 of Omi-S virus bearing the NTD, RBD, or RBM of WA1 (**Fig. 4d**). The neutralization assay showed
182 that mutations in the RBM were the major cause of Omicron's resistance to vaccine-induced
183 humoral immunity: replacing the RBM of WA1 with that of Omicron decreased ND₅₀ by 5.4-fold (p
184 < 0.0001), and conversely, substituting the RBM of Omi-S with that of WA1 increased ND₅₀ by
185 5.6-fold ($p = 0.0003$) (**Fig. 4c,d**). The fact that none of the RBM-swap viruses achieved the
186 difference of ~11-fold seen between WA1 and Omi-S suggests that mutations in other parts of S
187 also contribute to vaccine resistance.

188 To investigate if specific mutations in Omicron RBM drive vaccine escape, we
189 generated two additional panels of recombinant viruses, one with WA1 spike carrying Omicron
190 RBM mutations, either singly or in combination (**Fig. 4e**), and the other with Omicron spike lacking
191 the same set of mutations (**Fig. 4f**). Two WA1 mutants, mutant 3 (carrying E484A substitution)
192 and mutant 4 (bearing a cluster of five substitutions Q493R, G496S, Q498R, N501Y, Y505H)
193 exhibited a moderate but statistically significant decrease of 1.4-fold ($p = 0.0002$) and 1.8-fold (p
194 $= 0.0003$) in ND₅₀ values, respectively, compared with WA1 (**Fig. 4e**). The opposite was observed

195 when these mutations were removed from Omicron S; the Omicron mutant 3 (lacking E484A
196 substitution) and mutant 4 (lacking Q493R, G496S, Q498R, N501Y, Y505H) had a 1.9-fold ($p =$
197 0.0082) and 3.1-fold ($p = 0.0025$) higher ND_{50} values compared with Omicron (**Fig. 4f**). Since
198 none of the mutants captured the overall phenotype of Omicron, we assume that the vaccine
199 escape is a cumulative effect of mutations distributed along the length of the S protein. It is
200 possible that mutations alter the conformation of Omicron S in such a manner that most of the
201 immunodominant neutralizing epitopes are disrupted and become unavailable for neutralization.

202 **DISCUSSION**

203 This study provides important insights into Omicron pathogenicity. We show that spike, the
204 single most mutated protein in Omicron, has an incomplete role in Omicron attenuation. In *in vitro*
205 infection assays, the Omicron spike-bearing ancestral SARS-CoV-2 (Omi-S) exhibits much higher
206 replication efficiency compared with Omicron. Similarly, in K18-hACE2 mice, Omi-S contrasts with
207 non-fatal Omicron and causes a severe disease leading to around 80% mortality. This suggests
208 that mutations outside of spike are major determinants of the attenuated pathogenicity of Omicron
209 in K18-hACE2 mice. Further studies are needed to identify those mutations and decipher their
210 mechanisms of action.

211 One potential limitation of our study is the use of K18-hACE2 mice for pathogenesis studies
212 instead of the primate models that have more similarities with humans^{52,53}. It should however be
213 noted that the K18-hACE2 mouse model is a well-established model for investigating the lethal
214 phenotype of SARS-CoV-2^{3,42,54-56}. While these mice develop lung pathology following SARS-
215 CoV-2 infection, mortality has been associated with central nervous system involvement due to
216 viral neuroinvasion^{42,57}. The fact that infection with Omi-S, but not with Omicron, elicits neurologic

217 signs, such as hunched posture and lack of responsiveness, in K18-hACE2 mice suggests that
218 the neuroinvasion property is preserved in Omi-S, and the determinants of this property lie outside
219 of the spike protein.

220 We found that while the ancestral virus mainly replicates in lung alveoli and causes only
221 rare infection of bronchioles in K18-hACE2 mice, Omi-S with isogenic ancestral virus backbone
222 exhibits higher propensity to replicate in bronchiolar epithelium. This is consistent with a hamster
223 study demonstrating higher predilection of Omicron for bronchioles¹. In vitro studies have also
224 showed that while Omicron replicates poorly in lower lung cells⁵⁸, it causes a robust infection in
225 bronchiolar and nasal epithelial cells⁵⁸⁻⁶⁰. Our findings indicate that the higher preference of
226 Omicron for bronchioles is dictated by mutations in the spike protein. We speculate that both Omi-
227 S and Omicron enter the bronchiolar epithelium of K18-hACE2 mice, yet only Omi-S replicates to
228 high enough levels to manifest in overt bronchiolar injury. The preference of Omicron spike for
229 bronchiolar epithelium is likely mediated by its improved efficiency to utilize Cathepsin B/L⁵⁸⁻⁶²,
230 which form an active viral entry pathway in bronchioles and other airway cells^{59,63}. In contrast,
231 SARS-CoV-2 entry into alveolar epithelial cells is mainly driven by TMPRSS2^{36,64}, which Omicron
232 spike is deficient in utilizing^{60,65}, leading to poor infection of these cells^{3,37,58,60}. These findings
233 explain the higher transmission and lower lung pathology caused by Omicron.

234 Our study shows that mutations in the RBM of Omicron spike are the major determinants
235 of the viral escape from neutralizing antibodies, although mutations in other regions of spike also
236 contribute. Within the RBM, we identify two hotspots of mutations, which impart on Omicron spike
237 the ability to resist neutralization: one bearing the E484A substitution and the other harboring a
238 cluster of five substitutions, Q493R, G496S, Q498R, N501Y and Y505H. The E484A substitution

239 has been shown to escape neutralization by convalescent sera⁶⁶. Further, structural modeling
240 suggests that some therapeutic monoclonal antibodies establish highly stable salt bridges with
241 the E484 residue, entirely losing their binding when this residue is changed to A or upon Q493K
242 and Y505H changes⁶⁷. Similarly, mapping of RBM residues that directly interact with 49 known
243 neutralizing antibodies revealed N440, G446, S477, and T478 as low-frequently interactors,
244 N501, Y505, and Q498 as medium-frequency interactors, and E484 and Q493 as high-frequency
245 interactors⁶⁸, which is in line with our neutralization assay results. Interestingly, while antibody-
246 binding potential of Omicron spike is impaired⁶⁹, its receptor-binding capacity is intact. In fact, the
247 Omicron RBD has higher affinity for ACE2 relative to the Wuhan-Hu-1 and Delta RBDs⁶⁰. This
248 indicates that mutations in the Omicron spike have evolved in such a manner that they hinder
249 antibody binding but preserve the receptor engagement. This opens up the possibility of targeting
250 the conserved and structurally constrained regions of spike involved in ACE2 recognition for the
251 design of broad-spectrum vaccines to control the current COVID-19 pandemic.

252 **MATERIALS AND METHODS**

253 **Cells, antibodies, and plasmids**

254 The cell lines were incubated at 37°C and 5% CO₂ in a humidified incubator. Human
255 embryonic kidney HEK293T cells (ATCC; CRL-3216), human lung adenocarcinoma A549 cells
256 (ATCC; CCL-185), human colorectal adenocarcinoma Caco-2 cells (ATCC; HTB-37), and African
257 green monkey kidney Vero E6 cells were maintained in DMEM (Gibco; #11995-065) containing
258 10% FBS and 1X non-essential amino acids. Lentiviral delivery system was used to generate cells

259 stably expressing human ACE2 and TMPRSS2. Mycoplasma negative status of all cell lines was
260 confirmed.

261 Anti-SARS-CoV nucleocapsid (N) protein antibody (Rockland; #200-401-A50) was used
262 for detection of the SARS-CoV-2 N protein by IF. Expression plasmid encoding the spike protein
263 of the SARS-CoV-2 Wuhan isolate, pCSII-SARS-CoV-2 F8, was a kind gift from Yoshiharu
264 Matsuura³². We replaced the Wuhan spike in this plasmid with a chemically synthesized version
265 of Omicron spike and called the resulting plasmid pCSII-SARS-CoV-2 F8_Omicron. The lentiviral
266 vectors, pLOC_hACE2_PuroR and pLOC_hTMPRSS2_BlastR, containing human ACE2 and
267 TMPRSS2, respectively, have been previously described³³.

268 **Omicron stock preparation and titration**

269 All procedures were performed in a biosafety level 3 (BSL3) facility at the National
270 Emerging Infectious Diseases Laboratories of the Boston University using biosafety protocols
271 approved by the institutional biosafety committee (IBC). The SARS-CoV-2 BA.1 Omicron virus
272 stock was generated in ACE2/TMPRSS2/Caco-2 cells. Briefly, 5×10^5 cells, grown overnight in
273 DMEM/10%FBS/1X NEAA in one well of a 6-well plate, were inoculated with the collection
274 medium in which the nasal swab from a SARS-CoV-2 patient was immersed. The swab material
275 was obtained from the Department of Public Health, Massachusetts, and it contained the
276 sequence-verified Omicron virus (NCBI accession number: OL719310). Twenty-four hours after
277 infecting cells, the culture medium was replaced with 2 ml of DMEM/2%FBS/1X NEAA and the
278 cells were incubated for another 72h, at which point the CPE became visible. The culture medium
279 was harvested, passed through a 0.45μ filter, and kept at -80°C as a P0 virus stock. To generate
280 a P1 stock, we infected 1×10^7 ACE2/TMPRSS2/Caco-2 cells, seeded the day before in a T175

281 flask, with the P0 virus at an MOI of 0.01. The next day, the culture medium was changed to 25
282 ml of 2% FBS-containing medium. Three days later, when the cells exhibited excessive CPE, the
283 culture medium was harvested, passed through a 0.45 μ filter, and stored at -80°C as a P1 stock.

284 To titrate the virus stock, we seeded ACE2/TMPRSS2/Caco-2 cells into a 12-well plate at
285 a density of 2×10^5 cells per well. The next day, the cells were incubated with serial 10-fold
286 dilutions of the virus stock (250 μ l volume per well) for 1h at 37°C, overlaid with 1 ml per well of
287 medium containing 1:1 mixture of 2X DMEM/4% FBS and 1.2% Avicel (DuPont; RC-581), and
288 incubated at 37°C for another three days. To visualize the plaques, the cell monolayer was fixed
289 with 4% paraformaldehyde and stained with 0.1% crystal violet, with both fixation and staining
290 performed at room temperature for 30 minutes each. The number of plaques were counted and
291 the virus titer was calculated.

292 **Recombinant SARS-CoV-2 generation by CPER**

293 SARS-CoV-2 recombinant viruses were generated by using a modified form of the recently
294 published CPER protocol^{32,70}. Full-length SARS-CoV-2 cDNA cloned onto a bacterial artificial
295 chromosome (BAC)³⁰ was used as a template to amplify the viral genome into eight overlapping
296 fragments (F1, F2, F3, F4, F5, F6, F7, and F9). The pCSII-SARS-CoV-2 F8 and pCSII-SARS-
297 CoV-2 F8_Omicron plasmids, which were used to generate spike mutants, served as templates
298 for amplification of fragment 8 (F8). A UTR linker containing a hepatitis delta virus ribozyme
299 (HDVr), the bovine growth hormone polyadenylation signal sequence (BGH-polyA), and a
300 cytomegalovirus (CMV) promoter was cloned onto a pUC19 vector and used as a template to
301 amplify the linker sequence. The 5' termini of all ten DNA fragments (F1-F9 and the linker) were
302 phosphorylated by using T4 PNK (NEB; #M0201), and the equimolar amounts (0.05 pmol each)

303 of the resulting fragments were subjected to a CPER reaction in a 50 μ l volume using 2 μ l of
304 PrimeStar GXL DNA polymerase (Takara Bio; #R050A). The following cycling conditions were
305 used for CPER: an initial denaturation at 98°C for 2 min; 35 cycles of denaturation at 98°C for 10
306 s, annealing at 55°C for 15 s, and extension at 68°C for 15 min; and a final extension at 68°C for
307 15 min. The nicks in the circular product were sealed by using DNA ligase.

308 To transfect cells with the CPER product, we seeded ACE2/TMPRSS2/Caco-2 cells into a
309 6-well plate at a density of 5 x10⁵ cells per well. The transfection mix was prepared by mixing 26
310 μ l of the original 52 μ l CPER reaction volume with 250 μ l of Opti-MEM (Thermo Fisher Scientific;
311 #31985070) and 6 μ l of TransIT-X2 Dynamic Delivery System (Mirus Bio; #MIR 6000). Following
312 incubation at room temperature for 25 min, the transfection mix was added to the cells. The next
313 day, the culture medium was replaced with fresh DMEM containing 2% FBS. The CPE became
314 visible in 3-4 days, at which point the culture medium was collected and stored as a P0 virus
315 stock. The P0 stock was used for experiments described in this manuscript. The spike region of
316 all CPER-generated viruses was sequenced by either Sanger sequencing or next generation
317 sequencing to confirm the presence of desired and the absence of adventitious changes.

318 **SARS-CoV-2 neutralization assay**

319 For neutralization assays, initial 1:10 dilutions of plasma, obtained from individuals
320 who received two shots of either Moderna or Pfizer mRNA-based SARS-CoV-2 vaccine, were
321 five-fold serial diluted in Opti-MEM over seven or eight dilutions. These plasma dilutions were
322 then mixed at a 1:1 ratio with 1.25 x 10⁴ infectious units of SARS-CoV-2 and incubated for 1h at
323 37°C. Thereafter, 100 μ l of this mixture was directly applied to ACE2/A549 cells seeded the
324 previous day in poly-L-lysine-coated 96-well plates at a density of 2.5 x 10⁴ cells per well in 100

325 μ l volume. Thus, the final starting dilution of plasma was 1:20 and the final MOI was 0.5. The cells
326 were incubated at 37°C for 24h, after which they were fixed and stained with an anti-nucleocapsid
327 antibody. When PBS instead of plasma was used as a negative control, these infection conditions
328 resulted in around 40-50% infected cells at 24 hpi.

329 **Generation and infection of iAT2 cells**

330 The detailed protocol for generation of human iPSC-derived alveolar epithelial type II cells
331 (iAT2s) has been published in our recent papers^{36,71}. The air-liquid interface (ALI) cultures were
332 established by preparing single cell suspensions of iAT2 3D sphere cultures grown in Matrigel.
333 Briefly, Matrigel droplets containing iAT2 spheres were dissolved in 2 mg/ml dispase (Sigma) and
334 the spheres were dissociated in 0.05% trypsin (GIBCO) to generate a single-cell suspension. 6.5
335 mm Transwell inserts (Corning) were coated with dilute Matrigel (Corning) in accordance with the
336 manufacturer's protocol. Single-cell iAT2s were plated on Transwells at a density of 520,000
337 cells/cm² in 100 μ l of CK+DCI medium containing 10 μ M of Rho-associated kinase inhibitor ("Y";
338 Sigma Y-27632). 600 μ l of this medium was added to the basolateral compartment. 24h after
339 plating, the basolateral medium was changed with fresh CK+DCI+Y medium. 48h after plating,
340 the apical medium was aspirated to initiate ALI culture. 72h after plating, basolateral medium was
341 replaced with CK+DCI medium to remove the rho-associated kinase inhibitor. Basolateral medium
342 was changed every two days thereafter. The detailed composition of CK+DCI medium is provided
343 in our previous publications^{36,71}.

344 iAT2 cells in ALI cultures were infected with purified SARS-CoV-2 stock at an MOI of 2.5
345 based on the titration done on ACE2/TMPRSS2/Caco-2 cells. For infection, 100 μ l of inoculum
346 prepared in 1X PBS (or mock-infected with PBS-only) was added to the apical chamber of each

347 Transwell and incubated for 2h at 37°C followed by the removal of the inoculum and washing of
348 the apical side three times with 1X PBS (100 μ l/wash). The cells were incubated for two or four
349 days, after which the newly released virus particles on the apical side were collected by adding
350 100 μ l of 1X PBS twice to the apical chamber and incubating at 37°C for 15 min. The number of
351 infectious virus particles in the apical washes were measured by the plaque assay on
352 ACE2/TMPRSS2/Caco-2 cells. For flow cytometry, iAT2 cells were detached by adding 0.2 ml
353 Accutase (Sigma; #A6964) apically and incubated at room temperature for 15 min. The detached
354 cells were pelleted by low-speed centrifugation, fixed in 10% formalin, and stained with anti-
355 SARS-CoV-2 N antibody.

356 **Mice maintenance and approvals**

357 Mice was maintained in a facility accredited by the Association for the Assessment and
358 Accreditation of Laboratory Animal Care (AAALAC). Animal studies were performed following the
359 recommendations in the Guide for the Care and Use of Laboratory Animals of the National
360 Institutes of Health. The protocols were approved by the Boston University Institutional Animal
361 Care and Use Committee (IACUC). Heterozygous K18-hACE2 C57BL/6J mice (Strain 2B6.Cg-
362 Tg(K18-ACE2)2PrImn/J) were purchased from the Jackson Laboratory (Jax, Bar Harbor, ME).
363 Animals were housed in ventilated cages (Tecniplast, Buguggiate, Italy) and maintained on a
364 12:12 light cycle at 30-70% humidity, ad-libitum water, and standard chow diets (LabDiet, St.
365 Louis, MO).

366 **Mice infection**

367 Twelve to twenty weeks old male and female K18-hACE2 mice were inoculated intranasally
368 with 10^4 PFU of SARS-CoV-2 in 50 μ l of sterile 1X PBS. The inoculations were performed under

369 1-3% isoflurane anesthesia. Twenty-six mice (6 for WT, 10 for Omi-S, and 10 for Omicron) were
370 enrolled in a 14-day survival study, and another 42 mice (14 for each of the WT, Omi-S, and
371 Omicron viruses) were used for virological and histological analysis of infected lungs. During the
372 survival study, the animals were monitored for body weight, respiration, general appearance,
373 responsiveness, and neurologic signs. An IACUC-approved clinical scoring system was used to
374 monitor disease progression and define humane endpoints. The score of 1 was given for each of
375 the following situations: body weight, 10-19% loss; respiration, rapid and shallow with increased
376 effort; appearance, ruffled fur and/or hunched posture; responsiveness, low to moderate
377 unresponsiveness; and neurologic signs, tremors. The sum of these individual scores constituted
378 the final clinical score. Animals were considered moribund and humanly euthanized in case of
379 weight loss greater than or equal to 20%, or if they received a clinical score of 4 or greater for two
380 consecutive days. Body weight and clinical score were recorded once per day for the duration of
381 the study. For the purpose of survival curves, animals euthanized on a given day were counted
382 dead the day after. Animals found dead in cage were counted dead on the same day. For
383 euthanization, an overdose of ketamine was administered followed by a secondary method of
384 euthanization.

385 For quantification of SARS-CoV-2 infectious particles in lungs by the plaque assay, lung
386 tissues were collected in 600 μ l of RNAlater stabilization solution (ThermoFisher Scientific;
387 #AM7021) and stored at -80°C until analysis. 20-40 mg of tissue was placed in a tube containing
388 600 μ l of OptiMEM and a 5 mm stainless steel bead (Qiagen; #69989) and homogenized in the
389 Qiagen TissueLyser II by two dissociation cycles (1,800 oscillations/minute for 2 minutes) with a
390 one-minute interval between cycles. The homogenate was centrifuged at 15,000 xg for 10 minutes

391 at room temperature and the supernatant was transferred to a new tube. Ten-fold serial dilutions
392 of this supernatant were used for the plaque assay on ACE2/TMPRSS2/Caco-2 cells, as
393 described above.

394 For IHC and histologic analysis, the insufflated whole lung tissues were inactivated in 10%
395 neutral buffered formalin at a 20:1 fixative to tissue ratio for a minimum of 72h before removal
396 from BSL3 in accordance with an approved IBC protocol. Tissues were subsequently processed,
397 embedded in paraffin and five-micron sections stained with hematoxylin and eosin (H&E) following
398 standard histological procedures. IHC was performed using a Ventana BenchMark Discovery
399 Ultra autostainer (Roche Diagnostics, USA). An anti-SARS-CoV-2 S antibody (Cell Signaling
400 technologies: clone E5S3V) that showed equivalent immunoreactivity against WT and Omicron
401 spike was used to identify virus-infected cells. Negative and positive controls for IHC included
402 blocks of uninfected and SARS-CoV-2-infected Vero E6 cells, respectively.

403 **Flow cytometry**

404 For flow cytometry, fixed cells were permeabilized in 1x permeabilization buffer
405 (ThermoFisher Scientific; #00-5523-00) and stained with SARS-CoV-2 nucleocapsid antibody
406 (Rockland; #200-401-A50, 1:1,000), followed by donkey anti-rabbit IgG-AF647 secondary
407 antibody (ThermoFisher Scientific; #A-31573). Gating was based on uninfected stained control
408 cells. The extent of staining was quantified using a BD LSR II flow cytometer (BD Biosciences,
409 CA), and the data were analyzed with FlowJo v10.6.2 (FlowJo, Tree Star Inc).

410 **Immunofluorescence**

411 Immunofluorescence was performed as described in our previous publication³³. Briefly,
412 virus-infected cells were fixed in 4% paraformaldehyde and permeabilized in a buffer containing
413 0.1% Triton X-100 prepared in PBS. Following blocking in a buffer containing 0.1% Triton X-100,
414 10% goat serum, and 1% BSA, the cells were incubated overnight at 4°C with anti-SARS-CoV
415 Nucleocapsid antibody (1:2,000 dilution). The cells were then stained with Alexa Fluor 568-
416 conjugated goat anti-rabbit secondary antibody (1:1000 dilution) (Invitrogen; #A11008) in the dark
417 at room temperature for 1h and counterstained with DAPI. Images were captured using the
418 ImageXpress Micro Confocal (IXM-C) High-Content Imaging system (Molecular Devices) with a
419 4x S Fluor objective lens at a resolution of 1.7 micron/pixel in the DAPI (excitation: 400 nm/40 nm,
420 emission: 447 nm/60 nm) and TexasRed (excitation: 570nm/80nm, emission: 624nm/40nm)
421 channels. Both channels were used to establish their respective laser autofocus offsets. The
422 images were analyzed using MetaXpress High Content Image Acquisition and Analysis software
423 (Molecular Devices). First, the images were segmented using the CellScoring module. The
424 objects between 7 and 20 microns in diameter and greater than 1800 gray level units in intensity
425 were identified and classified as nuclei. Positive cells were taken as nuclei having TexasRed
426 signal of 1500 gray level units or above within 10 to 20 microns of each nucleus. The remaining
427 objects were set to negative cells. From these objects, the following readouts were measured and
428 used for downstream analysis: Total number of positive and negative cells, total area of positive
429 cells, and integrated intensity in the TexasRed channel for positive cells. To calculate the 50%
430 neutralizing dilution (ND₅₀), we performed a non-linear regression curve fit analysis using Prism 9
431 software (GraphPad).

432 **ACKNOWLEDGEMENT**

433 We thank Dr. Yoshiharu Matsuura from Osaka University, Japan, for providing the pCSII-
434 SARS-CoV-2 F8 plasmid; the Department of Public Health, Massachusetts, for providing the
435 clinical specimen containing Omicron virus; and the ICCB-Longwood Screening Facility of
436 Harvard Medical School for assistance with IF image acquisition and analysis. This work was
437 supported by Boston University startup funds (to MS and FD), National Institutes of Health, NIAID
438 grants R01 AI159945 (to SB and MS) and R37 AI087846 (to MUG), NIH SIG grants S10-
439 OD026983 and SS10-OD030269 (to NAC), Peter Paul Career Development Award (to FD), and
440 BMBF SenseCoV2 01KI20172A (AE) and DFG Fokus COVID-19, EN 423/7-1 (AE). We thank the
441 Clinical & Translational Science Institute (CTSI; 1UL1TR001430) and Evans Center for
442 Interdisciplinary Biomedical Research at Boston University School of Medicine for their support of
443 the Affinity Research Collaborative on ‘Respiratory Viruses: A Focus on COVID-19’.

444 **AUTHOR CONTRIBUTIONS**

445 M.S. conceptualized the study. DYC, AHT, DK, CVC, NK, HLC, FD, and MS performed
446 experiments. GL and MUG established and provided the modified CPER system. NAC performed
447 histopathologic and IHC analysis of mouse lungs. SCB and MB provided scientific input and
448 helped secure funds. AH and AE provided BAC harboring the SARS-CoV-2 genome. JHC
449 provided the Omicron isolate. YK provided plasma samples. MS wrote the manuscript, which was
450 read, edited, and approved by all authors.

451

452

453

454

455 **REFERENCES**

- 456 1 Suzuki, R. *et al.* Attenuated fusogenicity and pathogenicity of SARS-CoV-2 Omicron variant.
457 *Nature*, doi:10.1038/s41586-022-04462-1 (2022).
- 458 2 Halfmann, P. J. *et al.* SARS-CoV-2 Omicron virus causes attenuated disease in mice and hamsters.
459 *Nature*, doi:10.1038/s41586-022-04441-6 (2022).
- 460 3 Shuai, H. *et al.* Attenuated replication and pathogenicity of SARS-CoV-2 B.1.1.529 Omicron.
461 *Nature*, doi:10.1038/s41586-022-04442-5 (2022).
- 462 4 Dejnirattisai, W. *et al.* SARS-CoV-2 Omicron-B.1.1.529 leads to widespread escape from
463 neutralizing antibody responses. *Cell* **185**, 467-484 e415, doi:10.1016/j.cell.2021.12.046 (2022).
- 464 5 VanBlargan, L. A. *et al.* An infectious SARS-CoV-2 B.1.1.529 Omicron virus escapes
465 neutralization by therapeutic monoclonal antibodies. *Nat Med*, doi:10.1038/s41591-021-01678-y
466 (2022).
- 467 6 Planas, D. *et al.* Considerable escape of SARS-CoV-2 Omicron to antibody neutralization. *Nature*,
468 doi:10.1038/s41586-021-04389-z (2021).
- 469 7 Liu, L. *et al.* Striking antibody evasion manifested by the Omicron variant of SARS-CoV-2. *Nature*,
470 doi:10.1038/s41586-021-04388-0 (2021).
- 471 8 Hoffmann, M. *et al.* The Omicron variant is highly resistant against antibody-mediated
472 neutralization: Implications for control of the COVID-19 pandemic. *Cell* **185**, 447-456 e411,
473 doi:10.1016/j.cell.2021.12.032 (2022).
- 474 9 WHO. *Tracking SARS-CoV-2 variants*, <[https://www.who.int/en/activities/tracking-SARS-CoV-2-](https://www.who.int/en/activities/tracking-SARS-CoV-2-variants/)
475 [variants/](https://www.who.int/en/activities/tracking-SARS-CoV-2-variants/)> (2022).
- 476 10 Cele, S. *et al.* Omicron extensively but incompletely escapes Pfizer BNT162b2 neutralization.
477 *Nature* **602**, 654-656, doi:10.1038/s41586-021-04387-1 (2022).
- 478 11 Gu, H. *et al.* Probable Transmission of SARS-CoV-2 Omicron Variant in Quarantine Hotel, Hong
479 Kong, China, November 2021. *Emerg Infect Dis* **28**, 460-462, doi:10.3201/eid2802.212422 (2022).
- 480 12 Iuliano, A. D. *et al.* Trends in Disease Severity and Health Care Utilization During the Early
481 Omicron Variant Period Compared with Previous SARS-CoV-2 High Transmission Periods -
482 United States, December 2020-January 2022. *MMWR Morb Mortal Wkly Rep* **71**, 146-152,
483 doi:10.15585/mmwr.mm7104e4 (2022).
- 484 13 CDC. *COVID Data Tracker*, <<https://covid.cdc.gov/covid-data-tracker/#variant-proportions>>
485 (2022).
- 486 14 CoVariants. *CoVariants*, <<https://covariants.org>> (2022).
- 487 15 Taylor, L. Covid-19: Omicron drives weekly record high in global infections. *BMJ* **376**, o66,
488 doi:10.1136/bmj.o66 (2022).
- 489 16 Desingu, P. A. & Nagarajan, K. SARS-CoV-2 Omicron variant is spreading in different parts of the
490 world in three different trends. *J Med Virol*, doi:10.1002/jmv.27646 (2022).
- 491 17 WHO. Statement on Omicron sublineage BA.2. (2022).
- 492 18 Desingu, P. A. & Nagarajan, K. Omicron variant losing its critical mutations in the receptor-binding
493 domain. *J Med Virol*, doi:10.1002/jmv.27667 (2022).
- 494 19 Desingu, P. A., Nagarajan, K. & Dhama, K. Emergence of Omicron third lineage BA.3 and its
495 importance. *J Med Virol*, doi:10.1002/jmv.27601 (2022).
- 496 20 Takashita, E. *et al.* Efficacy of Antibodies and Antiviral Drugs against Covid-19 Omicron Variant.
497 *N Engl J Med*, doi:10.1056/NEJMc2119407 (2022).

- 498 21 Schmidt, F. *et al.* Plasma Neutralization of the SARS-CoV-2 Omicron Variant. *N Engl J Med* **386**,
499 599-601, doi:10.1056/NEJMc2119641 (2022).
- 500 22 ImperialCollegeLondon. *Hospitalisation risk for Omicron cases in England*,
501 <[https://www.imperial.ac.uk/mrc-global-infectious-disease-analysis/covid-19/report-50-severity-](https://www.imperial.ac.uk/mrc-global-infectious-disease-analysis/covid-19/report-50-severity-omicron/)
502 [omicron/](https://www.imperial.ac.uk/mrc-global-infectious-disease-analysis/covid-19/report-50-severity-omicron/)> (2022).
- 503 23 Madhi, S. A. *et al.* Population Immunity and Covid-19 Severity with Omicron Variant in South
504 Africa. *N Engl J Med*, doi:10.1056/NEJMoa2119658 (2022).
- 505 24 Sigal, A. Milder disease with Omicron: is it the virus or the pre-existing immunity? *Nat Rev*
506 *Immunol* **22**, 69-71, doi:10.1038/s41577-022-00678-4 (2022).
- 507 25 Wolter, N. *et al.* Early assessment of the clinical severity of the SARS-CoV-2 omicron variant in
508 South Africa: a data linkage study. *Lancet* **399**, 437-446, doi:10.1016/S0140-6736(22)00017-4
509 (2022).
- 510 26 Dyer, O. Covid-19: Omicron is causing more infections but fewer hospital admissions than delta,
511 South African data show. *BMJ* **375**, n3104, doi:10.1136/bmj.n3104 (2021).
- 512 27 Haseltine, W. A. in *Understanding Omicron: Changes In The Spike Protein And Beyond And What*
513 *They Portend* (2021).
- 514 28 Smyth, D. S. *et al.* Tracking cryptic SARS-CoV-2 lineages detected in NYC wastewater. *Nat*
515 *Commun* **13**, 635, doi:10.1038/s41467-022-28246-3 (2022).
- 516 29 Kirby, A. E. *et al.* Notes from the Field: Early Evidence of the SARS-CoV-2 B.1.1.529 (Omicron)
517 Variant in Community Wastewater - United States, November-December 2021. *MMWR Morb*
518 *Mortal Wkly Rep* **71**, 103-105, doi:10.15585/mmwr.mm7103a5 (2022).
- 519 30 Herrmann, A. *et al.* Cloning of a Passage-Free SARS-CoV-2 Genome and Mutagenesis Using Red
520 Recombination. *Int J Mol Sci* **22**, doi:10.3390/ijms221910188 (2021).
- 521 31 Amarilla, A. A. *et al.* A versatile reverse genetics platform for SARS-CoV-2 and other positive-
522 strand RNA viruses. *Nat Commun* **12**, 3431, doi:10.1038/s41467-021-23779-5 (2021).
- 523 32 Torii, S. *et al.* Establishment of a reverse genetics system for SARS-CoV-2 using circular
524 polymerase extension reaction. *Cell Rep* **35**, 109014, doi:10.1016/j.celrep.2021.109014 (2021).
- 525 33 Chen, D. Y. *et al.* SARS-CoV-2 Disrupts Proximal Elements in the JAK-STAT Pathway. *J Virol*
526 **95**, e0086221, doi:10.1128/JVI.00862-21 (2021).
- 527 34 Mulay, A. *et al.* SARS-CoV-2 infection of primary human lung epithelium for COVID-19 modeling
528 and drug discovery. *Cell Rep* **35**, 109055, doi:10.1016/j.celrep.2021.109055 (2021).
- 529 35 Carcaterra, M. & Caruso, C. Alveolar epithelial cell type II as main target of SARS-CoV-2 virus
530 and COVID-19 development via NF-Kb pathway deregulation: A physio-pathological theory. *Med*
531 *Hypotheses* **146**, 110412, doi:10.1016/j.mehy.2020.110412 (2021).
- 532 36 Huang, J. *et al.* SARS-CoV-2 Infection of Pluripotent Stem Cell-Derived Human Lung Alveolar
533 Type 2 Cells Elicits a Rapid Epithelial-Intrinsic Inflammatory Response. *Cell Stem Cell* **27**, 962-
534 973 e967, doi:10.1016/j.stem.2020.09.013 (2020).
- 535 37 Halfmann, P. J. *et al.* SARS-CoV-2 Omicron virus causes attenuated disease in mice and hamsters.
536 *Nature*, doi:10.1038/s41586-022-04441-6 (2022).
- 537 38 Winkler, E. S. *et al.* SARS-CoV-2 infection of human ACE2-transgenic mice causes severe lung
538 inflammation and impaired function. *Nat Immunol* **21**, 1327-1335, doi:10.1038/s41590-020-0778-
539 2 (2020).
- 540 39 Chen, R. E. *et al.* In vivo monoclonal antibody efficacy against SARS-CoV-2 variant strains. *Nature*
541 **596**, 103-108, doi:10.1038/s41586-021-03720-y (2021).
- 542 40 Cecon, E. *et al.* Therapeutic potential of melatonin and melatonergic drugs on K18-hACE2 mice
543 infected with SARS-CoV-2. *J Pineal Res* **72**, e12772, doi:10.1111/jpi.12772 (2022).

- 544 41 Lutz, C., Maher, L., Lee, C. & Kang, W. COVID-19 preclinical models: human angiotensin-
545 converting enzyme 2 transgenic mice. *Hum Genomics* **14**, 20, doi:10.1186/s40246-020-00272-6
546 (2020).
- 547 42 Mariano Carossino, D. K., Aoife K. O'Connell, Paige Montanaro, Anna E. Tseng, Hans P. Gertje,
548 Kyle A. Grosz, Maria Ericsson, Bertrand R. Huber, Susanna A. Kurnick, Saravanan Subramaniam,
549 Thomas A. Kirkland, Joel R. Walker, Kevin P. Francis, Alexander D. Klose, Neal Paragas, Markus
550 Bosmann, Mohsan Saeed, Udeni B. R. Balasuriya, Florian Douam, Nicholas A. Crossland Fatal
551 Neurodissemination and SARS-CoV-2 Tropism in K18-hACE2 Mice Is Only Partially Dependent
552 on hACE2 Expression. *Viruses* **14** (2022).
- 553 43 Ai, J. *et al.* Omicron variant showed lower neutralizing sensitivity than other SARS-CoV-2 variants
554 to immune sera elicited by vaccines after boost. *Emerg Microbes Infect* **11**, 337-343,
555 doi:10.1080/22221751.2021.2022440 (2022).
- 556 44 Huang, Y., Yang, C., Xu, X. F., Xu, W. & Liu, S. W. Structural and functional properties of SARS-
557 CoV-2 spike protein: potential antiviral drug development for COVID-19. *Acta Pharmacol Sin* **41**,
558 1141-1149, doi:10.1038/s41401-020-0485-4 (2020).
- 559 45 Lan, J. *et al.* Structure of the SARS-CoV-2 spike receptor-binding domain bound to the ACE2
560 receptor. *Nature* **581**, 215-220, doi:10.1038/s41586-020-2180-5 (2020).
- 561 46 Cerutti, G. *et al.* Potent SARS-CoV-2 neutralizing antibodies directed against spike N-terminal
562 domain target a single supersite. *Cell Host Microbe* **29**, 819-833 e817,
563 doi:10.1016/j.chom.2021.03.005 (2021).
- 564 47 Chi, X. *et al.* A neutralizing human antibody binds to the N-terminal domain of the Spike protein of
565 SARS-CoV-2. *Science* **369**, 650-655, doi:10.1126/science.abc6952 (2020).
- 566 48 Voss, W. N. *et al.* Prevalent, protective, and convergent IgG recognition of SARS-CoV-2 non-RBD
567 spike epitopes. *Science* **372**, 1108-1112, doi:10.1126/science.abg5268 (2021).
- 568 49 Premkumar, L. *et al.* The receptor binding domain of the viral spike protein is an immunodominant
569 and highly specific target of antibodies in SARS-CoV-2 patients. *Sci Immunol* **5**,
570 doi:10.1126/sciimmunol.abc8413 (2020).
- 571 50 Ju, B. *et al.* Human neutralizing antibodies elicited by SARS-CoV-2 infection. *Nature* **584**, 115-
572 119, doi:10.1038/s41586-020-2380-z (2020).
- 573 51 Piccoli, L. *et al.* Mapping Neutralizing and Immunodominant Sites on the SARS-CoV-2 Spike
574 Receptor-Binding Domain by Structure-Guided High-Resolution Serology. *Cell* **183**, 1024-1042
575 e1021, doi:10.1016/j.cell.2020.09.037 (2020).
- 576 52 Vogel, A. B. *et al.* BNT162b vaccines protect rhesus macaques from SARS-CoV-2. *Nature* **592**,
577 283-289, doi:10.1038/s41586-021-03275-y (2021).
- 578 53 Chang, M. C., Hild, S. & Grieder, F. Nonhuman primate models for SARS-CoV-2 research:
579 Consider alternatives to macaques. *Lab Anim (NY)* **50**, 113-114, doi:10.1038/s41684-021-00755-6
580 (2021).
- 581 54 Oladunni, F. S. *et al.* Lethality of SARS-CoV-2 infection in K18 human angiotensin-converting
582 enzyme 2 transgenic mice. *Nat Commun* **11**, 6122, doi:10.1038/s41467-020-19891-7 (2020).
- 583 55 Yinda, C. K. *et al.* K18-hACE2 mice develop respiratory disease resembling severe COVID-19.
584 *PLoS Pathog* **17**, e1009195, doi:10.1371/journal.ppat.1009195 (2021).
- 585 56 Gan, E. S. *et al.* A mouse model of lethal respiratory dysfunction for SARS-CoV-2 infection.
586 *Antiviral Res* **193**, 105138, doi:10.1016/j.antiviral.2021.105138 (2021).
- 587 57 Kumari, P. *et al.* Neuroinvasion and Encephalitis Following Intranasal Inoculation of SARS-CoV-
588 2 in K18-hACE2 Mice. *Viruses* **13**, doi:10.3390/v13010132 (2021).

- 589 58 Hui, K. P. Y. *et al.* SARS-CoV-2 Omicron variant replication in human bronchus and lung ex vivo. *Nature*, doi:10.1038/s41586-022-04479-6 (2022).
- 591 59 Thomas P. Peacock, J. C. B., Jie Zhou, Nazia Thakur, Joseph Newman, Ruthiran Kugathasan, Ksenia Sukhova, Myrsini Kaforou, Dalan Bailey, Wendy S. Barclay. The SARS-CoV-2 variant, Omicron, shows rapid replication in human primary nasal epithelial cultures and efficiently uses the endosomal route of entry. *bioRxiv*, doi:<https://doi.org/10.1101/2021.12.31.474653> (2022).
- 595 60 Meng, B. *et al.* Altered TMPRSS2 usage by SARS-CoV-2 Omicron impacts tropism and fusogenicity. *Nature*, doi:10.1038/s41586-022-04474-x (2022).
- 597 61 Du, X. *et al.* Omicron adopts a different strategy from Delta and other variants to adapt to host. *Signal Transduct Target Ther* **7**, 45, doi:10.1038/s41392-022-00903-5 (2022).
- 599 62 Pranesh Padmanabhan, N. M. D. Evidence of increased Cathepsin B/L and decreased TMPRSS2 usage for cell entry by the SARS-CoV-2 Omicron variant. *bioRxiv*, doi:<https://doi.org/10.1101/2022.01.13.476267> (2022).
- 602 63 Kawase, M., Shirato, K., van der Hoek, L., Taguchi, F. & Matsuyama, S. Simultaneous treatment of human bronchial epithelial cells with serine and cysteine protease inhibitors prevents severe acute respiratory syndrome coronavirus entry. *J Virol* **86**, 6537-6545, doi:10.1128/JVI.00094-12 (2012).
- 605 64 Grau-Exposito, J. *et al.* Evaluation of SARS-CoV-2 entry, inflammation and new therapeutics in human lung tissue cells. *PLoS Pathog* **18**, e1010171, doi:10.1371/journal.ppat.1010171 (2022).
- 607 65 Zhao, H. *et al.* SARS-CoV-2 Omicron variant shows less efficient replication and fusion activity when compared with Delta variant in TMPRSS2-expressed cells. *Emerg Microbes Infect* **11**, 277-283, doi:10.1080/22221751.2021.2023329 (2022).
- 610 66 Liu, Z. *et al.* Identification of SARS-CoV-2 spike mutations that attenuate monoclonal and serum antibody neutralization. *Cell Host Microbe* **29**, 477-488 e474, doi:10.1016/j.chom.2021.01.014 (2021).
- 613 67 Shah, M. & Woo, H. G. Omicron: A Heavily Mutated SARS-CoV-2 Variant Exhibits Stronger Binding to ACE2 and Potently Escapes Approved COVID-19 Therapeutic Antibodies. *Front Immunol* **12**, 830527, doi:10.3389/fimmu.2021.830527 (2021).
- 616 68 Ye, G., Liu, B. & Li, F. Cryo-EM structure of a SARS-CoV-2 omicron spike protein ectodomain. *Nat Commun* **13**, 1214, doi:10.1038/s41467-022-28882-9 (2022).
- 618 69 Carreno, J. M. *et al.* Activity of convalescent and vaccine serum against SARS-CoV-2 Omicron. *Nature* **602**, 682-688, doi:10.1038/s41586-022-04399-5 (2022).
- 620 70 Tamura, T. *et al.* Generation and characterization of genetically and antigenically diverse infectious clones of dengue virus serotypes 1-4. *Emerg Microbes Infect* **11**, 227-239, doi:10.1080/22221751.2021.2021808 (2022).
- 623 71 Jacob, A. *et al.* Derivation of self-renewing lung alveolar epithelial type II cells from human pluripotent stem cells. *Nat Protoc* **14**, 3303-3332, doi:10.1038/s41596-019-0220-0 (2019).

626 FIGURE LEGENDS

627 **Fig. 1: Generating Recombinant SARS-Co-2 by CPER.** a, Schematic overview of mutations in
628 Omicron spike (in comparison to the SARS-CoV-2 Wuhan-Hu-1 isolate; NCBI accession number:
629 NC_045512). Numbering is based on Wuhan-Hu-1 sequence. Mutations not reported in previous

630 variants of concern are shown in red. NTD, N-terminal domain; RBD, receptor-binding domain;
631 RBM, receptor-binding motif. **b**, Location of Omicron mutations on the trimeric spike protein.
632 Domains are colored according to a. **c**, Schematic of recombinant SARS-CoV-2 generated by
633 CPER. S, spike; N, nucleocapsid. **d**, ACE2/TMPRSS2/Caco-2 cells transfected with the SARS-
634 CoV-2 CPER product were stained with an anti-nucleocapsid antibody on indicated days post-
635 transfection. DAPI was used to stain the cell nuclei. NC, negative control generated by omitting
636 Fragment 9 from the CPER reaction. **e**, Virus titer in the culture medium of the transfected cells
637 at indicated days post-transfection, as measured by the plaque assay. The data are plotted as
638 mean \pm SEM of two experimental repeats.

639 **Fig. 2: Effect of spike on *in vitro* growth kinetics of Omicron.** **a**, Schematic of viruses used in
640 this figure. S, spike; N, nucleocapsid. **b-e**, ACE2/TMPRSS2/Caco-2 and Vero E6 cells were
641 infected at an MOI of 0.01, and the percentage of nucleocapsid (N)-positive cells ($n = 6$) (**b,c**) and
642 levels of infectious virus production ($n = 3$) (**d,e**) were determined by flow cytometry and the
643 plaque assay, respectively. **f**, The cell viability of SARS-CoV-2-infected ACE2/TMPRSS2/Caco-2
644 cells (MOI of 0.1) was quantified by the CellTiter-Glo assay at indicated time points. The *P* values
645 reflect a statistically significant difference between Omi-S and Omicron. **g**, Plaque sizes. Left,
646 representative images of plaques on ACE2/TMPRSS2/Caco-2 cells. Right, diameter of plaques
647 is plotted as mean \pm SD of 20 plaques per virus. **h**, Human induced pluripotent stem cell-derived
648 alveolar type 2 epithelial cells were infected at an MOI of 2.5 for 48h or 96h. The apical side of
649 cells was washed with 1X PBS and the levels of infectious virus particle were measured by the
650 plaque assay. $n = 4$. Data are mean \pm SD from the indicated number of biological replicates.
651 Experiments were repeated twice, with each experimental repeat containing 2 (**h**) or 3 (**b-g**)

652 replicates. p values were calculated by a two-tailed, unpaired t -test with Welch's correction. $*p$
653 <0.05 , $**p <0.01$, $***p <0.001$, and $****p < 0.0001$; ns, not significant.

654 **Fig. 3: Role of spike in Omicron pathogenicity.** **a-c**, Male and female K18-hACE2 mice (aged
655 12-20 weeks) were intranasally inoculated with 1×10^4 PFU of WT ($n = 6$), Omi-S ($n = 10$), or
656 Omicron ($n = 10$). Two independently generated virus stocks were used in this experiment. The
657 body weight (**a**), clinical score (**b**), and survival (**c**) were monitored daily for 14 days. Animals
658 losing 20% of their initial body weight were euthanized. **d,e**, K18-hACE2 mice were intranasally
659 inoculated with 1×10^4 PFU of WT ($n = 7$), Omi-S ($n = 7$), and Omicron ($n = 7$). Lung samples of
660 the infected mice were collected at 2 or 4 dpi to determine the viral titer ($n = 4$) (**d**) or for
661 immunohistochemistry (IHC) detection of the S protein ($n = 3$) (**e**). In **e**, representative images of
662 IHC staining for the detection of the SARS-CoV-2 S protein (brown color) in alveoli (arrows) and
663 bronchioles (arrowheads) in the lungs of the infected mice at 2 dpi are shown. (Scale bar = 100
664 μm). **f**, The percentage of S-positive bronchioles in the lungs of infected mice. Each dot represents
665 an infected animal. Data are presented as mean \pm SD from the indicated number of biological
666 replicates. Statistical significance was determined using two-tailed, unpaired t -test with Welch's
667 correction (**a,b,d,f**) and log-rank (Mantel-Cox) test (**c**). $*p <0.05$, $**p <0.01$, $***p <0.001$, and $****p$
668 < 0.0001 ; ns, not significant.

669 **Fig. 4: Role of spike in immune resistance of Omicron.** **a**, ND_{50} values for WA1, Omi-S, and
670 Omicron in sera from individuals who received two shots of Moderna (donor 1-12) or Pfizer (donor
671 13-24) vaccine (further details of sera are provided in Extended Data Table 1; individual curves
672 are shown in Extended Data Fig. 4). **b**, Trajectories of ND_{50} values against WA1, Omi-S, and
673 Omicron (the data from **a** is plotted). Fold-change in ND_{50} values is indicated. **c,d,e,f**, Schematic

674 of the chimeric (**top panels; c,d**) and mutant (**top panels; e,f**) viruses. The amino acid numbering
675 for WA1 mutants in e is based on the WA1 spike sequence, whereas the numbering for Omicron
676 mutants in f is based on the Omicron spike sequence. Six of the 24 sera (three from Moderna and
677 three from Pfizer) were tested. Each serum sample is represented by a dot of specific color. The
678 data are plotted as fold-change of the parental virus. Statistical significance was determined using
679 a two-tailed, unpaired *t* test with Welch's correction. **p* < 0.05, ***p* < 0.01, ****p* < 0.001, and *****p* <
680 0.0001; ns, not significant.

681 **EXTENDED DATA FIGURES**

682 **Extended Data Fig. 1: Schematic representation of CPER to generate recombinant SARS-**
683 **CoV-2.** The SARS-CoV-2 genome was amplified into nine overlapping fragments. These
684 fragments and a linker (containing a hepatitis delta virus ribozyme, a poly-A signal, and a CMV
685 promoter) were treated with PNK to phosphorylate 5' ends. The 5'-end phosphorylated fragments
686 were then stitched together by CPER, and the nicks in the resulting circular DNA molecule were
687 closed by treatment with DNA ligase. The CPER product was transfected into cells to rescue virus
688 particles.

689 **Extended Data Fig. 2: Clinical signs of Omi-S-infected mice.** K18-hACE2 mice (*n* = 10)
690 inoculated intranasally with 1 x 10⁴ PFU of Omi-S and described in Fig. 3a-c were monitored for
691 body weight (**a**) and clinical score (**b**). Animals losing 20% of their body weight (8 out of 10) were
692 euthanized. The surviving animals did not show any signs of distress.

693 **Extended Data Fig. 3: Lung pathology induced by Omi-S.** The lungs of the male and female
694 K18-hACE2 mice intranasally inoculated with 1 x 10⁴ PFU of WT, Omi-S, and Omicron were
695 collected at 2 dpi for histological analysis. **a**, Representative images of hematoxylin and eosin

696 (H&E) staining for the detection of bronchiolar damage in the lungs of the infected mice. The
697 bronchiolar epithelial necrosis is shown with arrows. Note that the necrosis was no longer evident
698 at 4 dpi in any cohort. **b**, Immunohistochemistry (IHC) staining for the detection of SARS-CoV-2
699 S protein in the same area where bronchiolar necrosis was seen. The only bronchiole found to be
700 positive for Omicron is shown. No evidence of necrosis was seen for this bronchiole. (Scale bar
701 = 100 μm).

702 **Extended Data Fig. 4: Individual neutralization data.** Individual neutralization curves for the
703 data presented in Fig. 4a,b are shown. The data represent the mean \pm SD of three technical
704 replicates. The curves were calculated based on a non-linear regression curve fit analysis in
705 Prism. The dotted lines represent the limit of detection.

706 **Extended Data Table 1:** Overview of serum samples used for the analysis of antibody
707 neutralization of WA1, Omi-S, and Omicron. *Days after the second vaccine shot. **The spike
708 antibody titer was measured by Abbott's SARS-CoV-2 immunoassays.

709

710

711

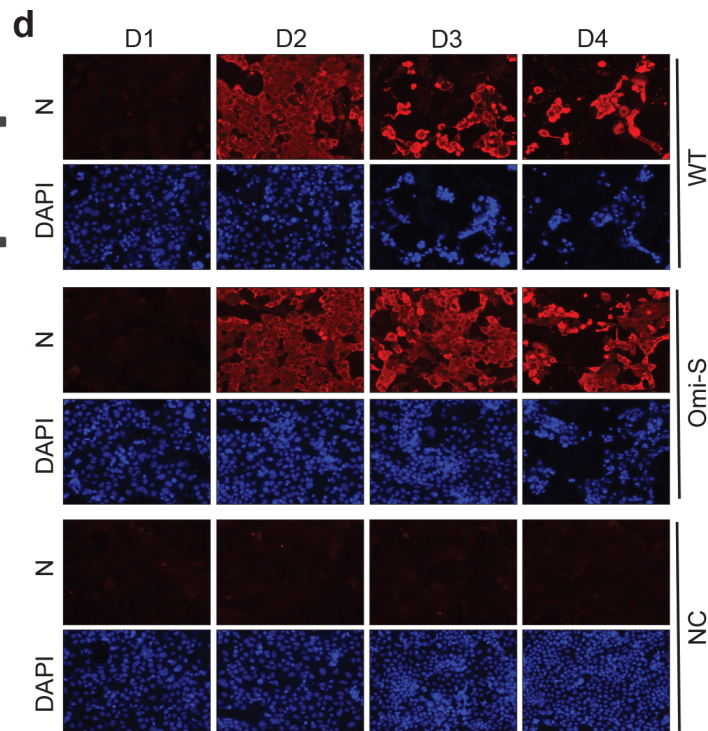
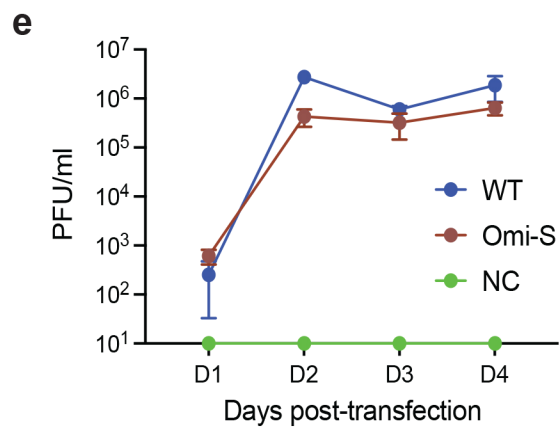
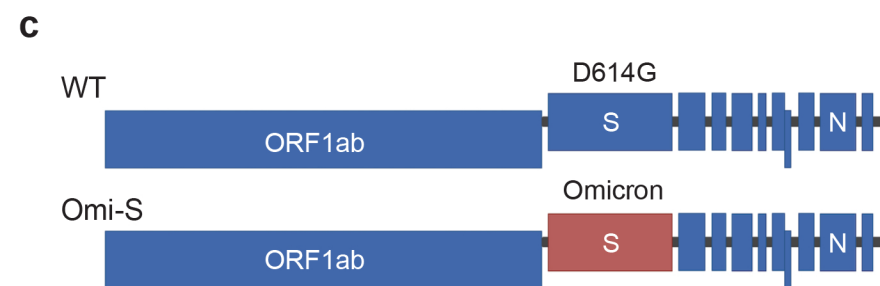
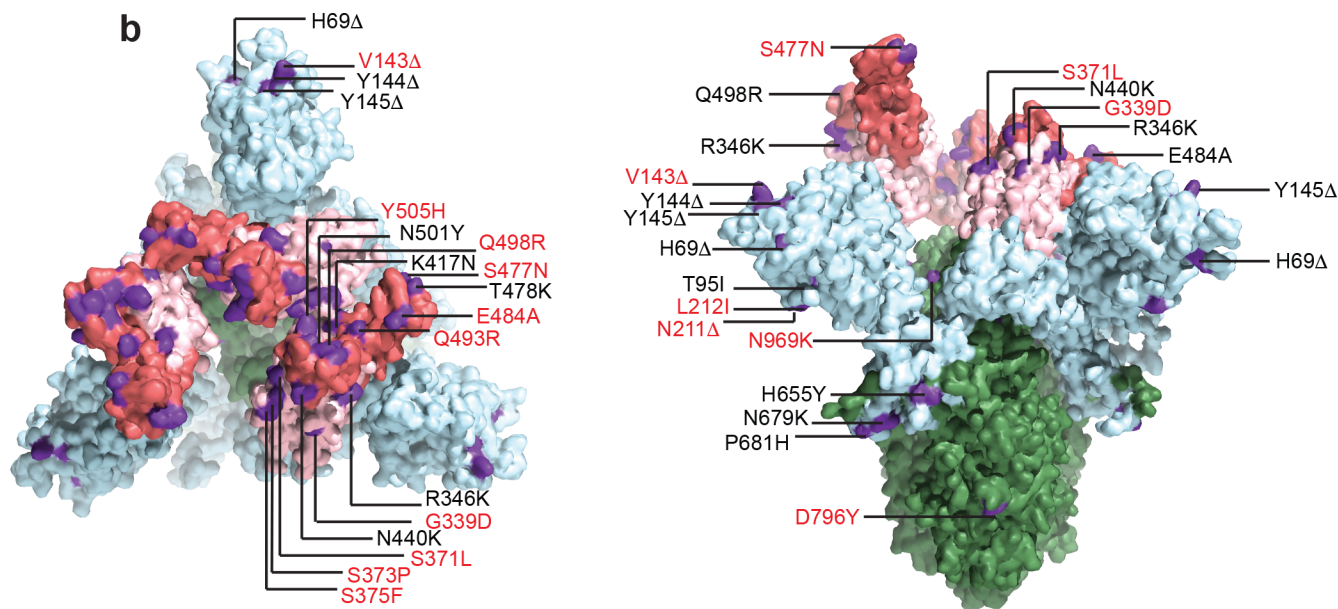
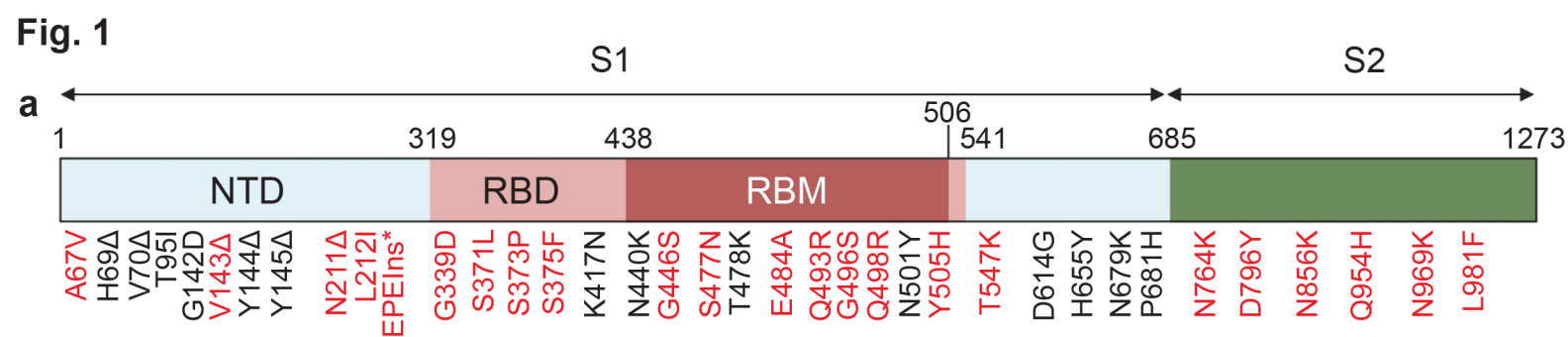


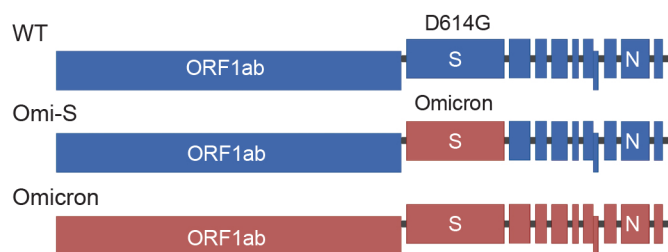
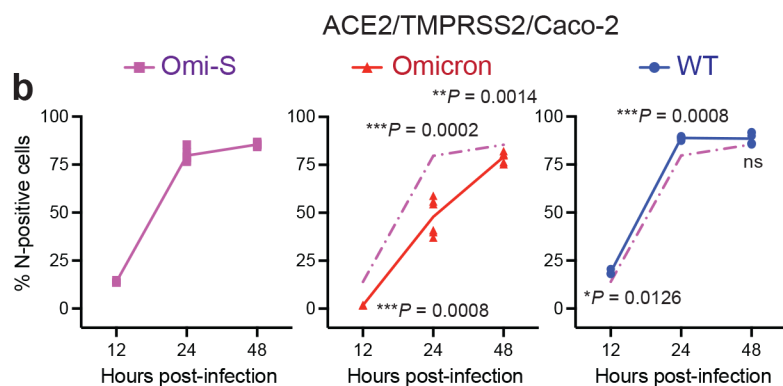
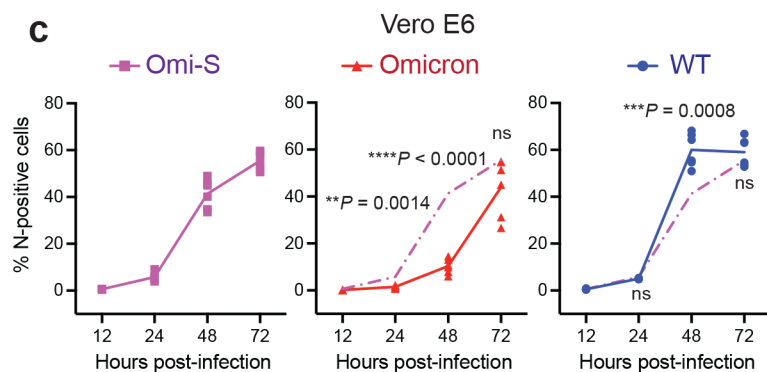
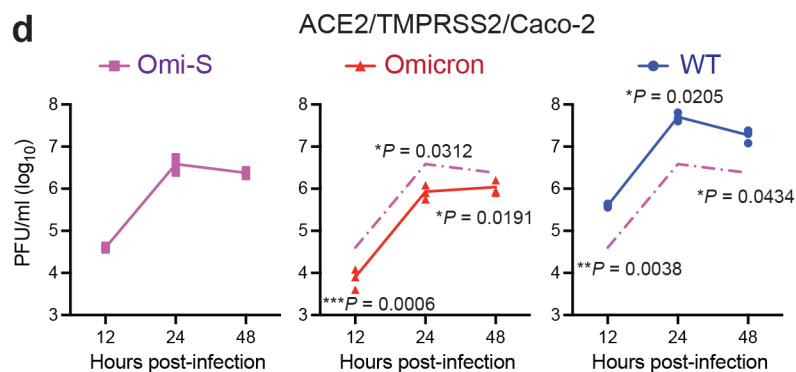
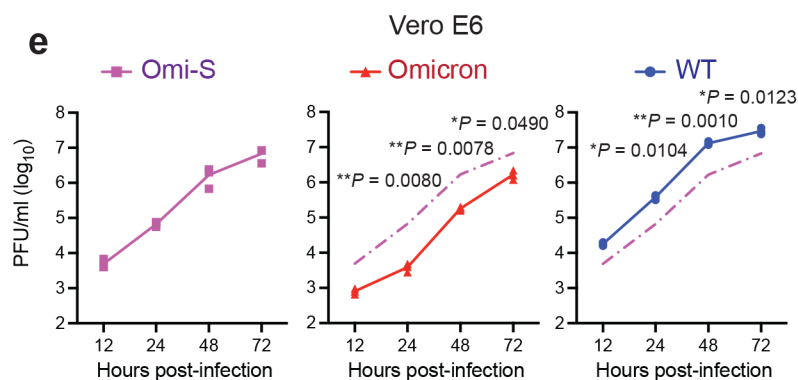
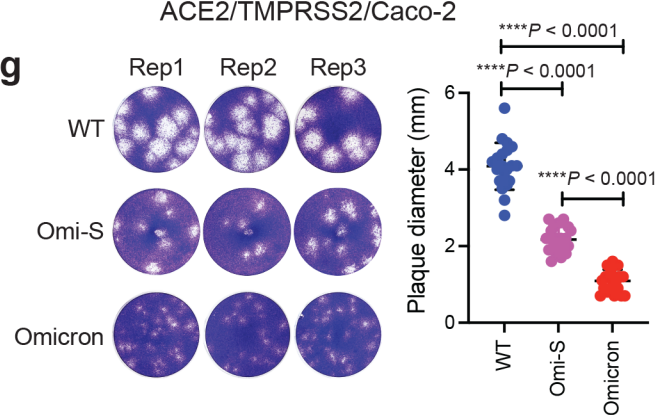
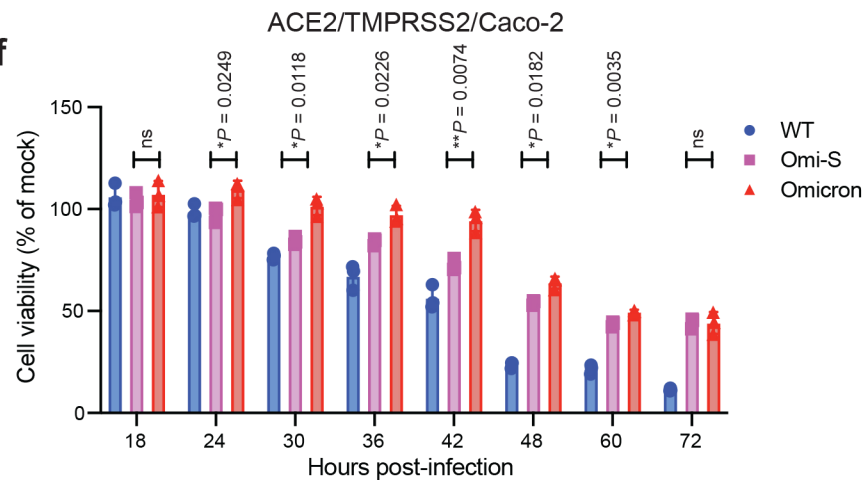
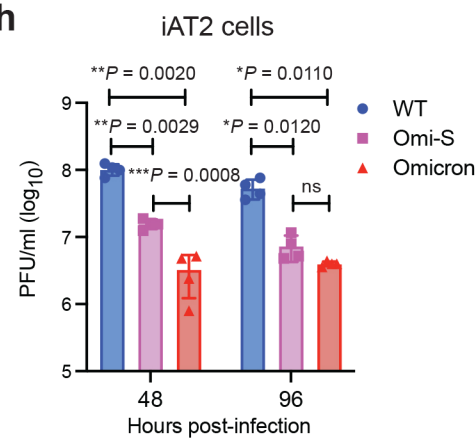
Fig. 2**a****b****c****d****e****g****f****h**

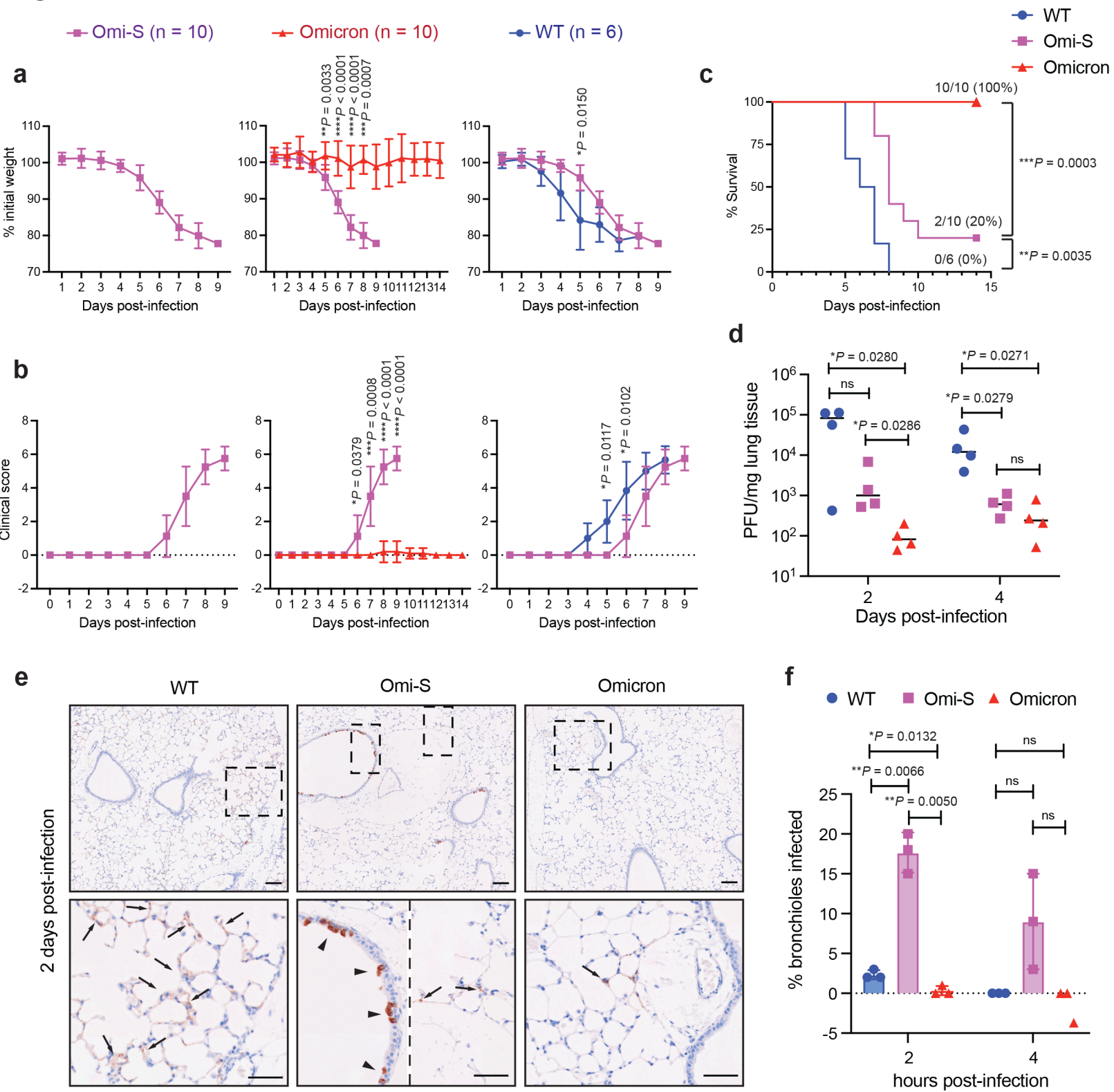
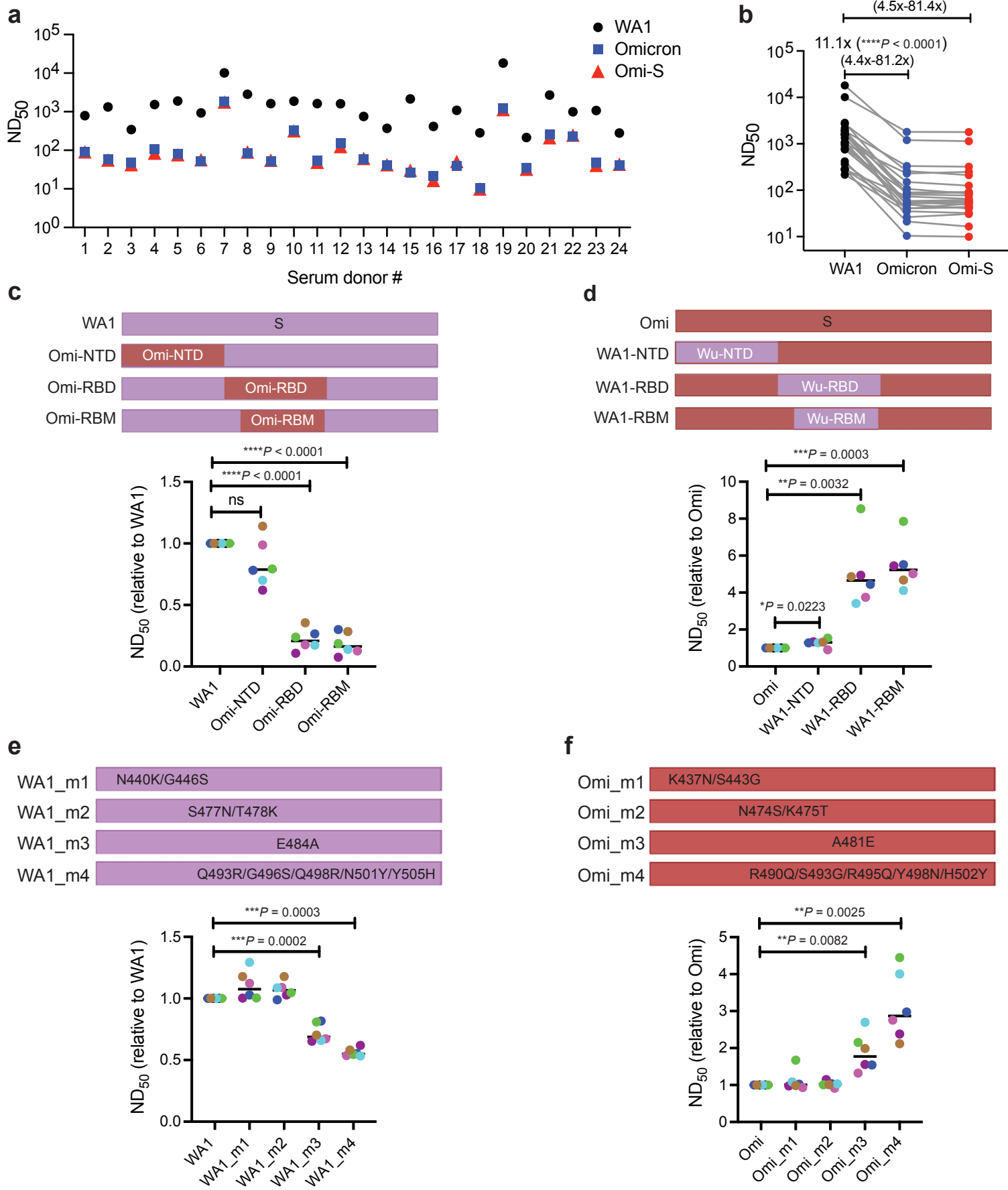
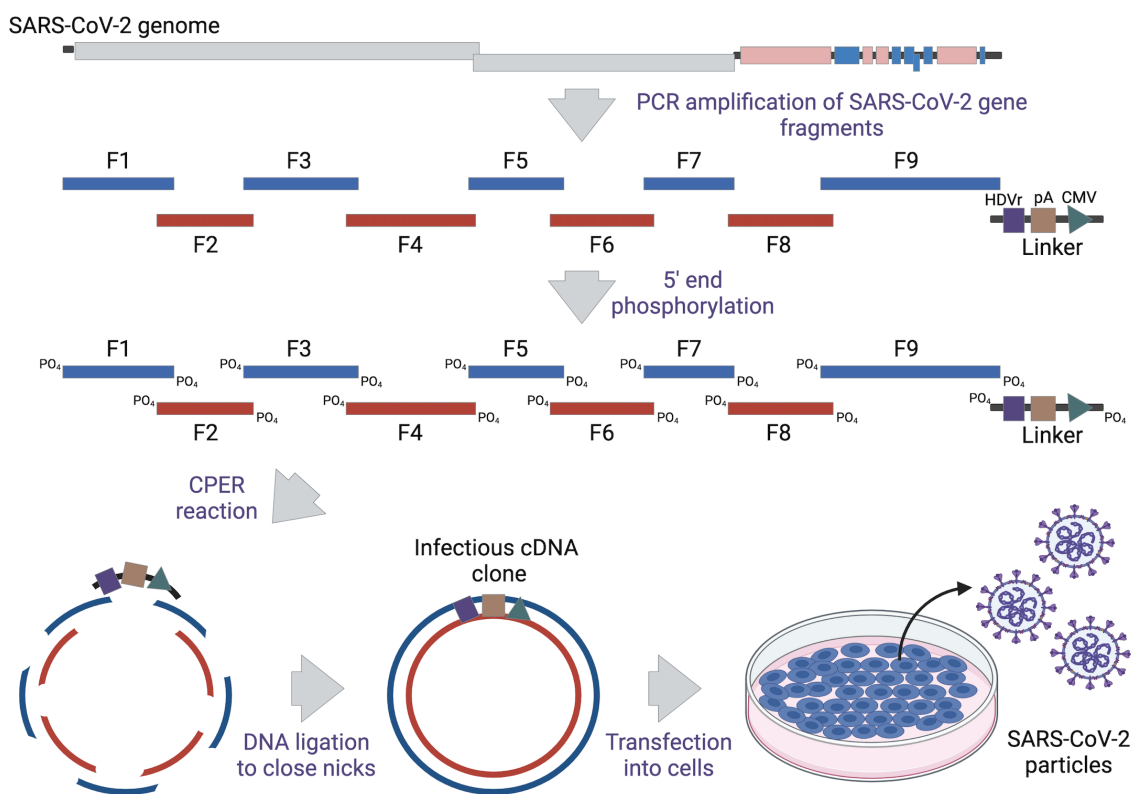
Fig. 3

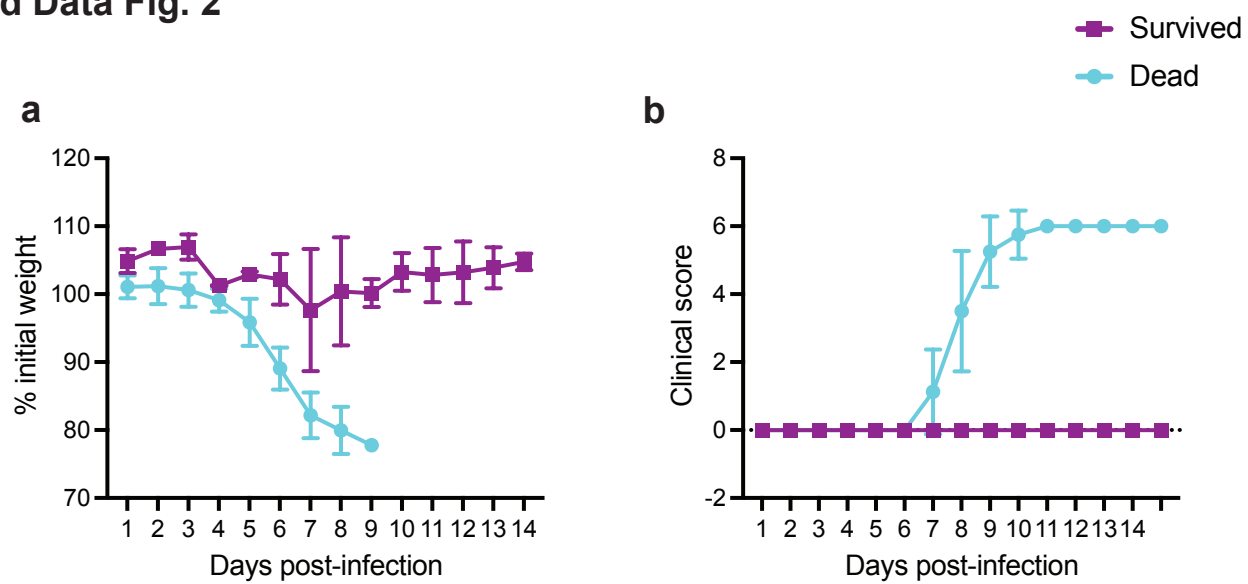
Fig. 4



Extended Data Fig. 1

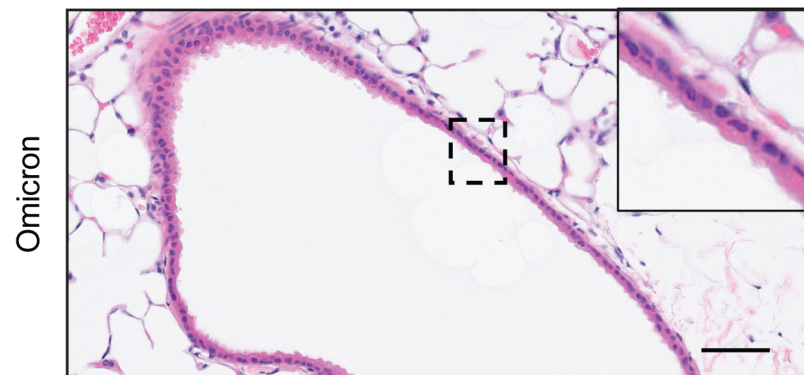
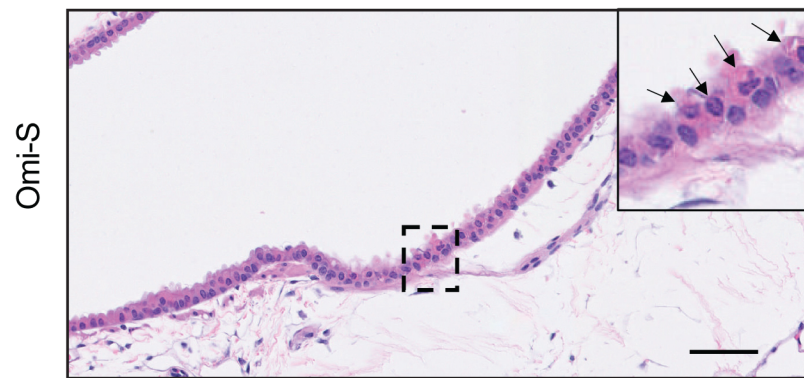
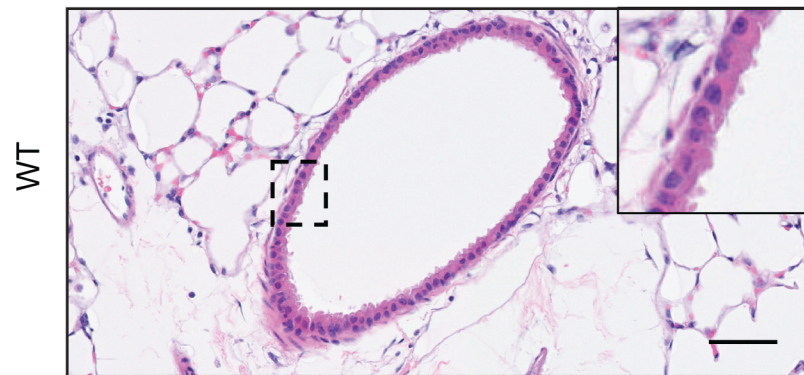


Extended Data Fig. 2

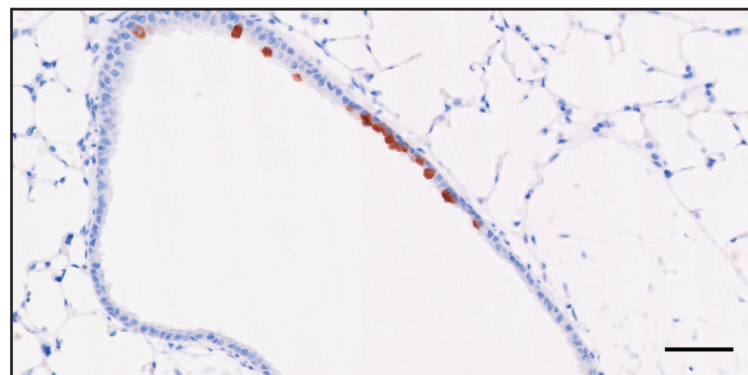
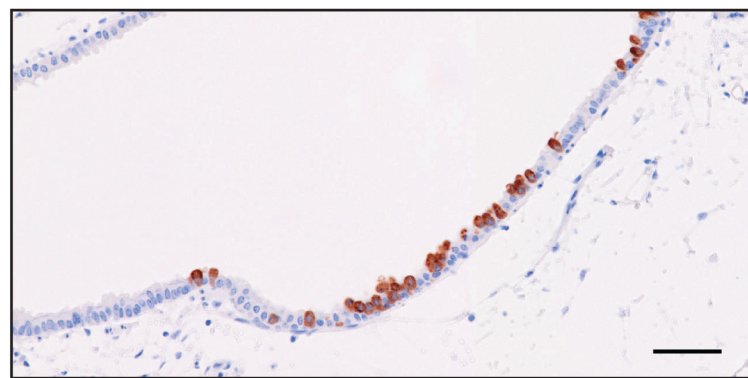
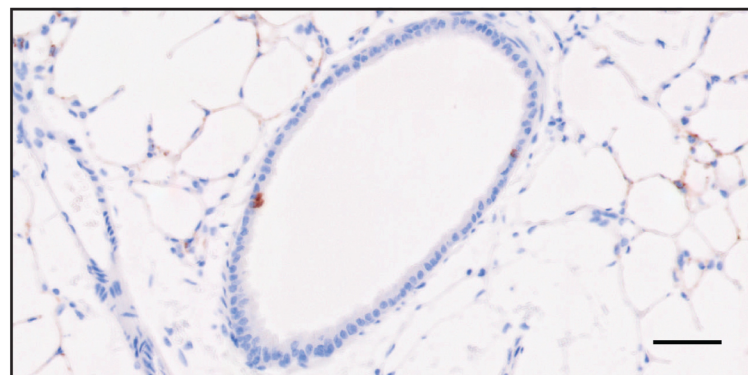


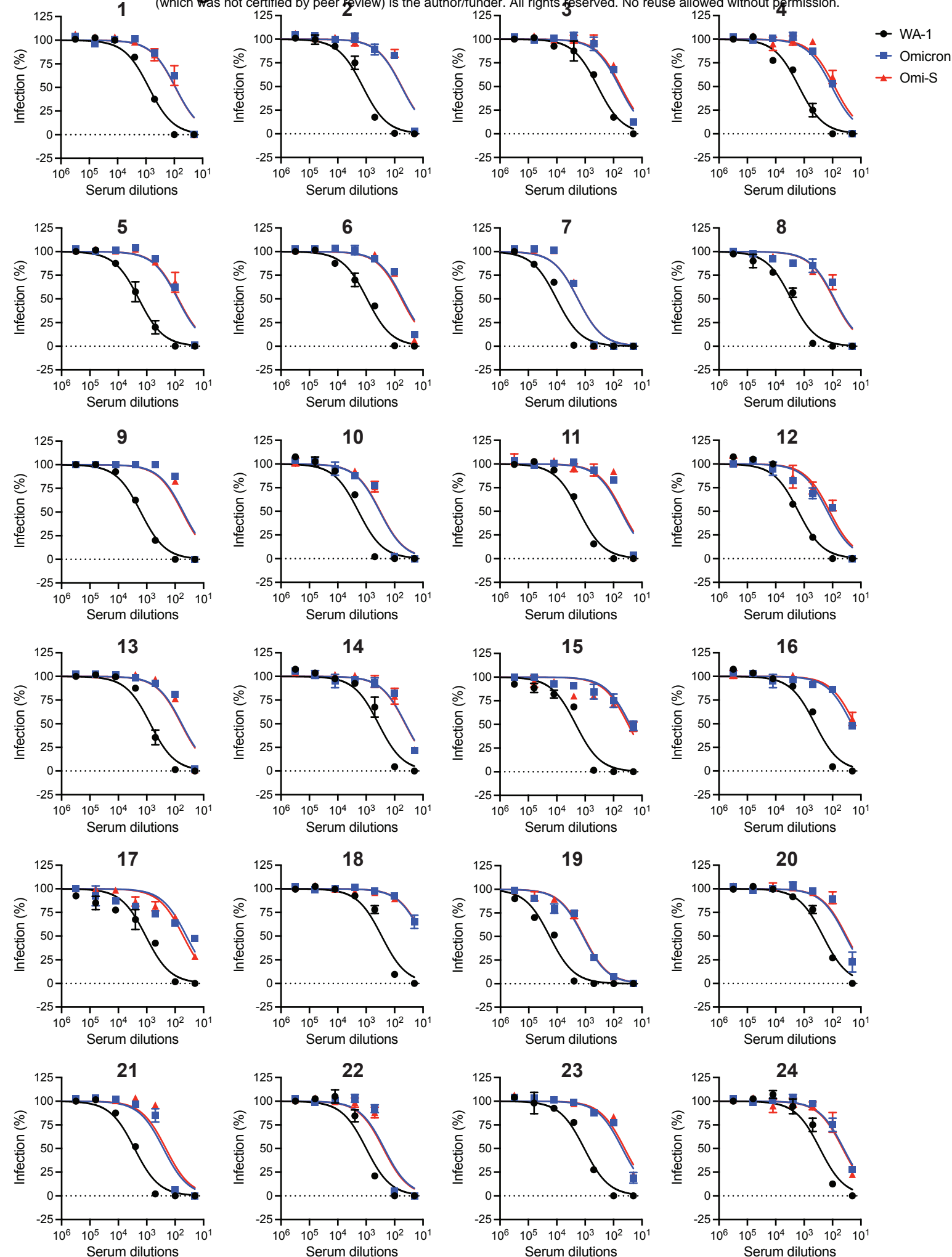
Extended Data Fig. 3

a



b





Extended Data Table 1

Serum no.	Sex	Race	Age	Days post-vaccination*	Vaccine (Manufacturer)	Spike Ab titer (AU/ml)**
1	Male	White	59	18	mRNA-1273 (Moderna)	39823.0
2	Male	Black	26	37	mRNA-1273 (Moderna)	26978.7
3	Male	Asian	55	34	mRNA-1273 (Moderna)	24880.7
4	Male	White	39	32	mRNA-1273 (Moderna)	23816.7
5	Male	Asian	45	38	mRNA-1273 (Moderna)	21659.5
6	Male	White	30	32	mRNA-1273 (Moderna)	18986.5
7	Female	Asian	47	35	mRNA-1273 (Moderna)	100000.0
8	Female	White	62	47	mRNA-1273 (Moderna)	69680.0
9	Female	White	39	14	mRNA-1273 (Moderna)	54996.6
10	Female	White	38	32	mRNA-1273 (Moderna)	46494.7
11	Female	White	34	30	mRNA-1273 (Moderna)	43784.0
12	Female	White	57	42	mRNA-1273 (Moderna)	42140.5
13	Male	Mixed	28	51	BNT162b2 (Pfizer-BioNTech)	17623.8
14	Male	White	30	54	BNT162b2 (Pfizer-BioNTech)	16154.5
15	Male	White	29	54	BNT162b2 (Pfizer-BioNTech)	14261.5
16	Male	Asian	48	48	BNT162b2 (Pfizer-BioNTech)	10593.6
17	Male	White	46	60	BNT162b2 (Pfizer-BioNTech)	9752.3
18	Male	White	31	53	BNT162b2 (Pfizer-BioNTech)	8715.2
19	Female	White	55	52	BNT162b2 (Pfizer-BioNTech)	100000.0
20	Female	White	43	47	BNT162b2 (Pfizer-BioNTech)	44385.4
21	Female	White	56	48	BNT162b2 (Pfizer-BioNTech)	39998.5
22	Female	Mixed	44	49	BNT162b2 (Pfizer-BioNTech)	31141.9
23	Female	White	56	50	BNT162b2 (Pfizer-BioNTech)	25969.6
24	Female	White	55	51	BNT162b2 (Pfizer-BioNTech)	23539.1